Separation and Purification Technology 304 (2023) 122312

Contents lists available at ScienceDirect

Separation and Purification Technology

journal homepage: www.elsevier.com/locate/seppur

An ultramicroporous metal-organic framework based on octahedral-like cages showing high-selective methane purification from a six-component C1/C2/C3 hydrocarbons mixture

Qiang Zhang [a], Xin Lian [a], Rajamani Krishna [b], Shan-Qing Yang [a], Tong-Liang Hu [a,*]

[a] School of Materials Science and Engineering, National Institute for Advanced Materials, Nankai University, Tianjin 300350, China
[b] Van 't Hoff Institute for Molecular Sciences, University of Amsterdam, Science Park 904, 1098 XH Amsterdam, The Netherlands

ARTICLE INFO

Keywords:
Metal-organic frameworks
Octahedral-like cages
CH_4 purification
C2-C3 hydrocarbons recovery
Adsorption mechanism research

ABSTRACT

Given the crucial significance of using cleaner methane (CH_4) to replace else fossil fuels in remitting energy consumption and preventing environmental degradation, developing prominent adsorbents to purify CH_4 from multicomponent mixtures is fundamentally important but faces great challenges. Cage-based metal-organic frameworks (MOFs) bring about widespread attention in solving numerous separation problems due to their inherent structural preponderances. Herein, we constructed an octahedral-like cages-based MOF (**NUM-18**) that incorporates two different types of cages within the whole framework and bears abundant Lewis basic sites (naked N atoms) and nonpolar aromatic rings immobilized in the pore surface. Benefitting from its intriguing structural characteristics, the pure-component gas adsorption properties were systematically investigated and indicate that **NUN-18a** (activated **NUM-18**) has excellent adsorptive capacities with respect to C2-C3 hydrocarbons than CH_4. The IAST adsorption selectivities for C2/CH_4 are above 14.0, while the adsorption selectivities of C3/CH_4 startlingly surpass 86.0, respectively, all of which forebode that **NUM-18a** can achieve efficient recovery of C2-C3 hydrocarbons associated with CH_4 purification. Furthermore, the actual separation feasibility for an equimolar 6-component C1/C2/C3 hydrocarbons mixture was examined by simulated dynamic column breakthrough experiments. Finally, molecular simulation calculations were adopted to ascertain potential gas adsorption mechanisms. This work provided a new paradigm for developing novel porous crystalline MOFs materials to separate hyper-complex gas mixtures.

1. Introduction

Along with the universal economy overgrowth, the increasingly serious environmental problems generated by the immoderate consumption of fossil energy have aroused widespread concerns, inducing a more exuberant demand for clean energy. As the principal component of natural gas, coal bed gas, shale gas, biogas, and refinery gas, methane (CH_4) was deemed to be one of the most important alternatives energy resources to gasoline or diesel automobile fuels, seeing its attractive accessibility and relatively eco-friendly peculiarity in comparison to other petrochemical fuel [1–3]. Depending on the differences in a variety of sources, there are always multiple undesirable impurities of C2-C3 light hydrocarbons (such as C_2H_6, C_2H_4, C_2H_2, C_3H_8, and C_3H_6) in naturally occurring CH_4 [4,5]. In another way, C2-C3 light hydrocarbons are vital raw materials for producing various important fine chemicals in the modern petrochemical industry [6]. Recovering such high value--added hydrocarbons from CH_4 to fully utilize them not only can improve the quality of CH_4 production to make it meet standard specifications, but can also increase the commercial values and combustion efficiency of these energy gases, which is a plan to kill two birds with one stone. However, the exceeding similarities of geometrical dimensions and boiling points for these gas molecules pose a formidable challenge for effective separation [7]. Typically, thermally driven cryogenic distillation and amine scrubbing are two of the main traditional methods for CH_4 purification in the process of industrial production, but they are frequently accompanied by high energy consumption, expensive input cost, harsh work conditions, and equipment corrosion [8]. Therefore, developing higher efficient and cleaner purification methods for CH_4 depuration is a very imperative task. Among the multitudinous newly developed technologies, the separation

* Corresponding author.
E-mail address: tlhu@nankai.edu.cn (T.-L. Hu).

https://doi.org/10.1016/j.seppur.2022.122312
Received 3 August 2022; Received in revised form 29 September 2022; Accepted 2 October 2022
Available online 9 October 2022

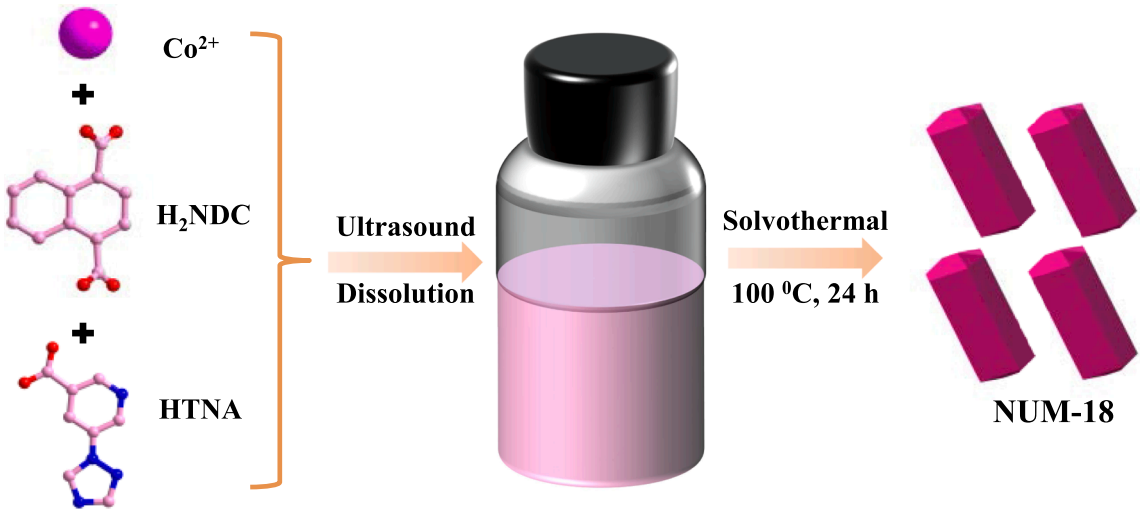

Fig. 1. Schematic illustration for self-assembly process of **NUM-18**.

with the aid of pressure-swing adsorption (PSA) through porous materials is considered an attractive alternative method to tackle these dilemmas, owing to its superiorities of low energy and cost investment [9]. It is noteworthy that the properties of porous adsorbents manifestly serve a primary role in PSA technology and mostly determine the ultimate separation efficiency. Nevertheless, the majority of traditional adsorbents (such as zeolites, carbon-based materials, and silica gels) show low porosity, restricted surface area, structural unicity, and lack of functional sites, and usually exhibit limited adsorption capacity and poor separation selectivity [10–12].

Metal-organic framework (MOF) materials, also known as porous coordination polymers, are identified as a subclass of burgeoning crystalline porous materials and can be straightforwardly self-assembled through metal ions (or metal clusters) as inorganic nodes and multidentate organic ligands as linkers, which reveals widespread applications in catalysis [13], chemical sensing [14], drug delivery [15], and so on. Especially, in the last 20 years, massive porous MOFs adsorbing materials have also been extensively used for gas storage and separation/purification schemes, ranging from H_2, CO_2, and C_2H_2 storage to high challenging alkyne/alkene and olefin/paraffin separation [16–19]. As to urgently anticipated CH_4 purification, although recent progress has also shown that porous MOFs are very promising candidates for separation of CH_4 from 2 to 4 component mixtures such as CO_2/CH_4 [20,21], C_2H_6/CH_4 [22,23], $C_2H_6/C_2H_2/CH_4$ [24], $C_2H_2/CO_2/CH_4$ [25], and $C_2H_2/C_2H_4/C_2H_6/CH_4$ [26], the separation of CH_4 from more complicated multivariate gas mixtures (≥5) has more crucial practical significance in the actual separation working conditions but is still rarely reported [27–30]. Simultaneously, in order to further improve the gas adsorption ability and separation selectivity, a variety of methods have been proposed to control pore size, functionalize pore surface, and tune structural flexibility. Among the above aspects, possessing the favorable pore size and shape for the MOFs sorbents is one of the foremost factors to achieve satisfied adsorption and separation performances. Through systematic adjusting aperture of MOFs to suit the gas molecular size can effectively boost the separation sieving effect and thus gain higher selectivity [31–33]. Moreover, modifying pore surface nature at the atomic level with various functional sites (such as –OH, $–NH_2$, SiF_6^{2-}) and Lewis acid/base sites to enhance adsorbate–surface interactions is another effective route to further improve the volumetric capacity and separation efficiency of MOF materials [34–36]. In this context, an effective strategy so-called dual functionalities was put forward, whose main focus is that both pore sizes and functional surfaces simultaneously enforce gas separations without the sacrifice of moderate pore volumes or surface areas to uptake large numbers of the preferred gas molecules [37–39]. Under the guidance of the dual-functionality strategy, synchronously optimizing the pore size and integrating appropriate functional sites toward targeted gas molecules has attained remarkable achievements in settling many pendant gas separation challenges.

As a distinguished category, cage-based MOFs differing from classical straight-channel MOFs adsorbing materials are ideal platforms to implement the dual-functionality strategy, because they possess large well-ordered cavities and small windows. In the aspect of criteria for pore size and space control, cage-based MOFs holding large cavity space but narrow windows sizes, are favorable to realize molecular sieve separation at the windows position and form molecule confinement effect between host framework and specific size molecules to remain dynamical trap inside the pore space [40–42]. Because the molecular sieving led by small window sizes often means the supernal selectivity and the large cavity space allows for high adsorption capacity, the cage-based MOFs are also very promising candidates for addressing the barriers of the trade-off between sorption capacity and separation selectivity. Otherwise, the strong host–guest interactions between cage-based MOFs and gas molecules also can be realized by employing proper functionalized regulation of the cage surface environment. Attracted by these unique benefits, the construction of desirable cage-based MOFs is eagerly aspiring, but is still a challenge for researchers. Tremendous efforts by our group have been devoted to exploring the design strategy and synthetic methodology toward the acquirement of novel cage-based MOFs for gas adsorption and separation application [43–45].

Herein, selecting a triangle ligand containing nicotinic acid and triazole moieties, which was assisted with linear dicarboxylic acid ligand, we constructed an octahedral-like cages-based Co-MOF $\{[Co_2(TNA)_2(NDC)(H_2O)]\cdot(DMF)_2\cdot(H_2O)_2\}_n$ (**NUM-18**) (HTNA = 5-(1*H*-1,2,4-triazol-1-yl)nicotinic acid, H_2NDC = 1,4-naphthalenedicarboxylic acid, DMF = *N*, *N*-dimethylformamide) (Fig. 1). There are two different kinds of cages in the **NUM-18** framework which exhibit large free voids with semblable inner diameters and small window sizes. Along the crystallographic [1 0 1] direction, two kinds of cages are arranged in the ABAB rule as the minimum repeat unit to constitute a tortuous channel. It is very satisfying to see, based on the results of the gas adsorption experiments, that **NUM-18a** (activated **NUM-18**) exhibits comparatively high adsorption capacity for C2-C3 light hydrocarbons and excellent selectivity for (C2/C3)/CH_4 in mixture gas. Note particularly, **NUM-18a** can separate CH_4 in ultrahigh purity from a complicated 6-component C1/C2/C3 gas mixture at room temperature, which has been established by the simulated breakthrough experiments. Structural analysis and GCMC simulations further indicate the underlying causes contributing to this admirable adsorption phenomenon and separation property. All results

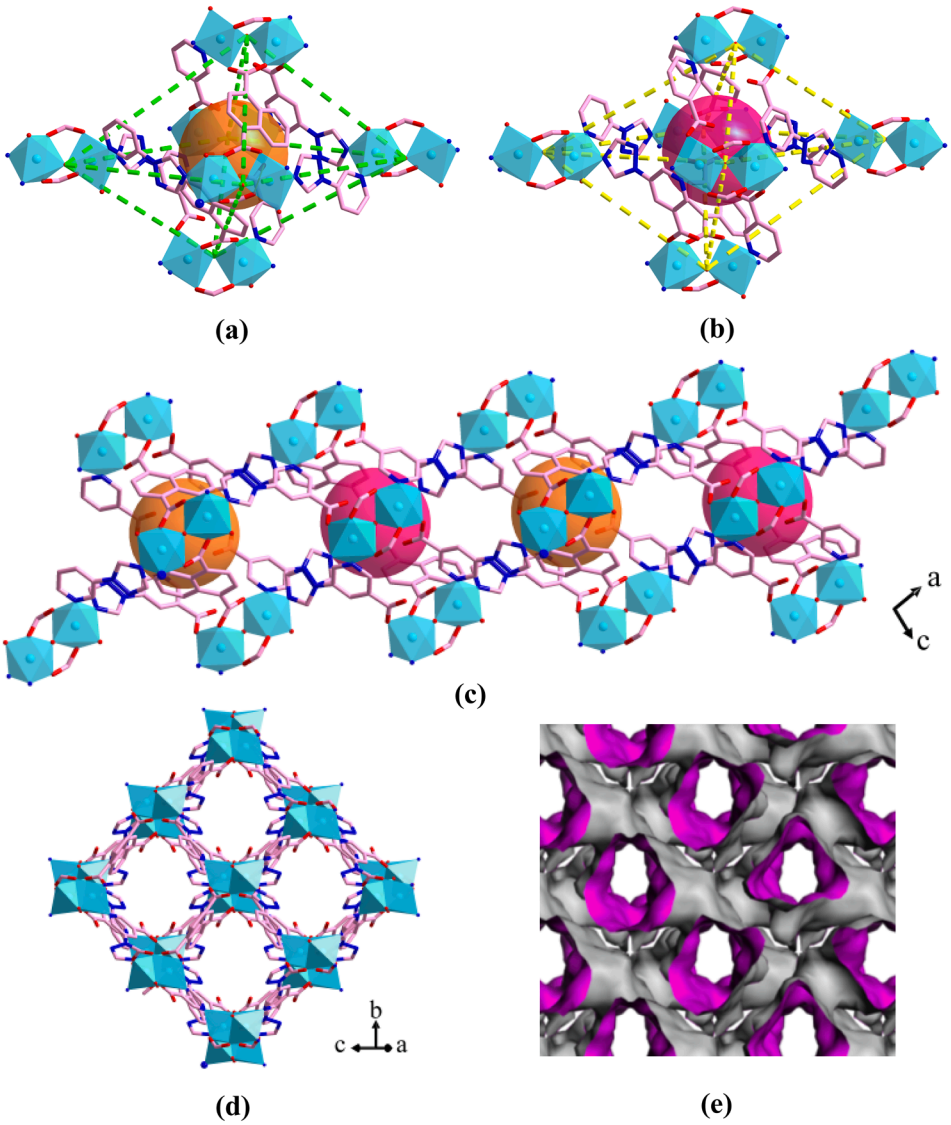

Fig. 2. (a) and (b) are two types of octahedral-like nanocages in **NUM-18**. (c) The single pore structure is constituted by the two types of octahedral-like nanocages in the ABAB arrangement view along the crystallographic *b* axis. (d) The channel structure is connected by octahedral-like nanocages and Connolly surface void spaces (e) of **NUM-18** view along the [1 0 1] direction. Color code: Co, sky blue; O, red; N, blue; C, rose. Guest molecules and H atoms have been omitted for clarity. (For interpretation of the references to color in this figure legend, the reader is referred to the web version of this article.)

of experiments and simulations show that **NUM-18a** is a promising selective adsorbent for PSA and can be applied to CH_4 purification under complicated working conditions.

2. Materials and methods

2.1. Materials and characterization

All chemicals and reagents were purchased from commercial suppliers and used without further purification. Powder X-ray diffraction (PXRD) and variable temperature powder X-ray diffraction (VT-PXRD) were measured on a Rigaku Miniflex 600 with Cu Kα radiation (λ = 1.5425 Å) under air conditions. The simulated PXRD pattern was calculated using Mercury software from the data of single-crystal X-ray diffraction structure. Thermogravimetric analysis (TGA) was recorded on a Rigaku standard thermogravimetry–differential thermal analysis (TG-DTA) analyzer utilizing an empty and clean Al_2O_3 crucible as reference (heating rate = 10 °C min^{-1} in Ar atmosphere). Elemental analysis (C, H, and N) was performed on a Vario EL cube elemental analyzer. IR spectra were measured in the range of 400–4000 cm^{-1} on a Tensor 37 OPUS FT-IR spectrometer (Bruker, German) using KBr pellets. Before the sorption measurement, the sample of **NUM-18** was soaked in anhydrous methanol for 3 days to exchange DMF and H_2O solvent molecules in the channels. The degas procedure for the methanol-exchanged **NUM-18** was conducted at 150 °C under a high vacuum ($<10^{-5}$ Torr) overnight and led to the formation of a completely activated sample **NUM-18a**. About 109.8 mg of the desolvated sample was used for the entire sorption measurements. The N_2 sorption isotherm measurement was carried out using a Micrometrics ASAP 2460 M volumetric gas adsorption analyzer at 77 K in a liquid-nitrogen bath. The CH_4, C_2H_6, and C_3H_8 sorption isotherm measurements were carried out at 273 and 298 K respectively in an ethanol bath using a Micrometrics ASAP 2460 M volumetric gas adsorption analyzer. Gas adsorption/desorption measurements of C_2H_4 and C_2H_2 were carried out using a Micrometrics ASAP 2020 M volumetric gas adsorption analyzer. The ultra-pure gases were used in all measurements.

2.2. Single-crystal X-ray diffraction study

Single-crystal data of **NUM-18** were recorded on a Rigaku XtaLAB PRO MM007 DW diffractometer with Cu Kα radiation (λ = 1.54184 Å) at 100(2) K. Absorption corrections by multi-scan were applied. The structure was solved with the *SHELXT* program and refined by full-matrix least-squares against F^2 using the *SHELXL* program [46,47]. Anisotropic thermal parameters were implemented to all non-hydrogen atoms, and all hydrogen atoms were placed in the calculated positions

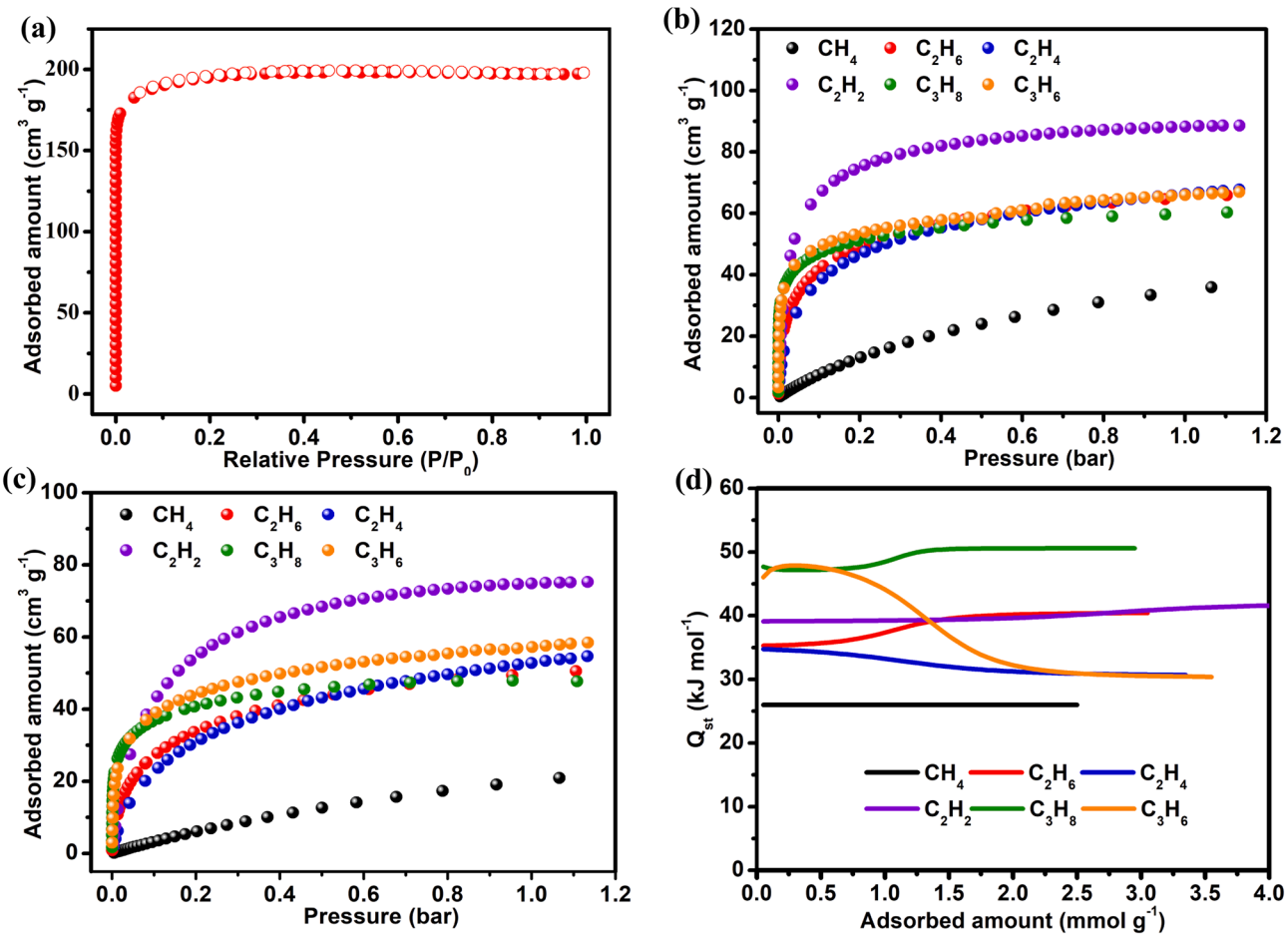

Fig. 3. (a) N_2 sorption isotherm of **NUM-18a** at 77 K. Gas adsorption isotherms of CH_4, C_2H_6, C_2H_4, C_2H_2, C_3H_8, and C_3H_6 for **NUM-18a** at (b) 273 K and (c) 298 K. (d) Isosteric enthalpy of adsorption of CH_4, C_2H_6, C_2H_4, C_2H_2, C_3H_8, and C_3H_6 in **NUM-18a**.

and refined with isotropic thermal parameters. *PLATON/SQUEEZE* was employed to remove scattering contributions of the disordered solvent molecules and the generated solvent-free data of direction intensities were further refined [48]. Details of the crystal parameters, data collection, and refinement of **NUM-18** are listed in Table S1.

2.3. Synthesis of NUM-18

A solvothermal reaction of $Co(NO_3)_2{\cdot}6H_2O$ (29.1 mg, 0.1 mmol), H_2NDC (11 mg, 0.05 mmol), and HTNA (19.0 mg, 0.1 mmol) in 3 mL of a mixed solvent of DMF/H_2O (2:1, v/v) was kept at 100 °C for 1 day, and pink clavate crystals of **NUM-18** were first time synthesized in 66 % yield based on the HTNA ligand (Fig. 1 and Fig. S1). When the reaction temperature slowly cooled to room temperature, fresh samples were collected by filtration and washed with fresh DMF several times. Selected IR data (KBr, cm^{-1}): 3439.83(m), 3101.67(w), 2360.83(w), 1668.99(s), 1627.83(s), 1413.03(m), 1392.59(m), 1365.86(m), 1029.04 (w), 787.88(w), 740.03(w), 670.32 (w) (Fig. S2). Elem anal.: Calcd for **NUM-18** ($C_{34}H_{38}N_{10}Co_2O_{14}$): C, 43.97; H, 4.09; N, 15.09. Found: C, 43.41; H, 3.77; N, 15.90.

3. Results and discussion

3.1. Single crystal X-ray diffraction structure

Single-crystal X-ray structure analysis revealed that **NUM-18** adopts a three-dimensional (3D) network that crystallizes in the monoclinic C2/c space group. The Co^{2+} atom demonstrates a hexacoordination mode and is connected to four oxygen atoms and two nitrogen atoms within distorted octahedron geometry. Further, two neighboring Co^{2+} atoms form the rare binuclear [$Co_2(\mu_2\text{-}OH_2)(COO)_2$] node through sharing bridged water molecule and two carboxylic groups, which can be regarded as a dual-core secondary building unit (SBU). Each binuclear SBU is linked by two $NDC2^-$ and six TNA^- ligands to give the 3D framework. An in-depth analysis of the structure showed that the entire 3D framework is constructed from the packing of the interlinked two types of distorted octahedral-like cages, which are built from six SBU units, two $NDC2^-$ ligands, and six TNA^- ligands (Fig. 2a, b). Both cages have a similar inner diameter of about 6 Å and a neck size of about 4 Å at the junction in the middle of both cages. As shown in Fig. 2c, the 1D twisted channel is constructed by two kinds of cages in an ABAB arrangement as the minimum repeat unit view in the [1 0 1] direction. Eventually, the adjacent individual channels are interconnected to form a 3D porous structure of **MUN-18** (Fig. 2d, e).

3.2. Stability analysis of NUM-18

The experimental and activated PXRD patterns are consistent well with the simulated one based on the single-crystal data, confirming the high phase purity and skeleton stability after degassing of **NUM-18** (Fig. S3). The thermostability was demonstrated by TGA and VT-PXRD. As shown in Fig.s S4 and S5, the skeleton of **NUM-18** remains stable up to 280 °C. Through testing PXRD of **NUM-18** soaked in various common solvents or exposure to air in the laboratory for 1 week (Fig. S6), it was found that **NUM-18** acquits itself well in solvent/air stability under different conditions.

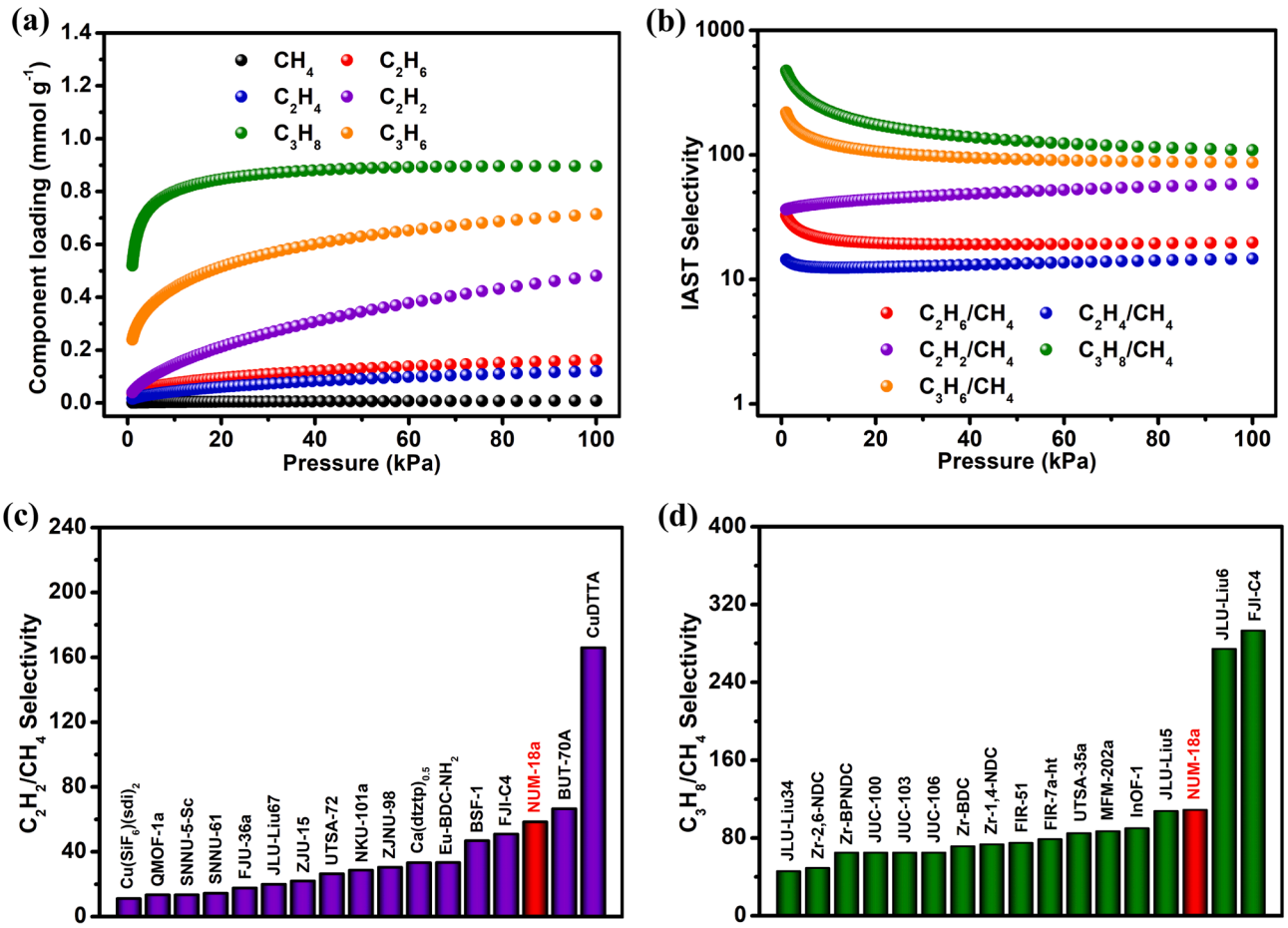

Fig. 4. (a) IAST calculations of component loadings for adsorption of 6-component $CH_4/C_2H_6/C_2H_4/C_2H_2/C_3H_8/C_3H_6$ gas mixtures in **NUM-18a** at 298 K. (b) IAST calculations of C_2H_6, C_2H_4, C_2H_2, C_3H_8, and C_3H_6 with respect to CH_4 in an equimolar 6-component mixture for **NUM-18a** at 298 K. Comparisons of (c) C_2H_2/CH_4 and (d) C_3H_8/CH_4 selectivities between **NUM-18a** and other reported MOFs.

3.3. Gas adsorption properties of NUM-18a

To assess the permanent porosity of **NUM-18a**, the N_2 sorption experiment at 77 K was carried out. The N_2 sorption profile shows an absolutely reversible type-I isotherm as expected for typical microporous materials, and the total N_2 uptake capacity was 198.0 $cm^3\ g^{-1}$ (Fig. 3a). Upon calculation according to the saturation uptake, the specific pore volume can be obtained, whose value reached 0.31 $cm^3\ g^{-1}$. Meanwhile, on the foundation of the N_2 adsorption result, an ultra-narrow pore-size distribution of about 3.71 Å can be gained through the Horvath-Kawazoe method, which ulteriorly indicates its ultra-microporous nature (Fig. S7). The Brunauer-Emmett-Teller (BET) and Langmuir surface area calculated from the N_2 isotherm was determined to be ~778.21 and 899.25 $m^2\ g^{-1}$, respectively (Figs. S8-S10).

The establishment of the large cavity space and intrinsic permanent porosity prompts us to evaluate its potential as an adsorbent for purifying CH_4 through the physisorption mechanism. To examine the sorption ability for light hydrocarbons of **NUM-18a**, the single-component gas sorption isotherms of C1-C3 hydrocarbon were recorded at both 273 and 298 K up to 1 bar. As shown in Fig. 3b and 3c, these pure-component gas adsorption isotherms revealed that the adsorption loadings at 273 and 298 K under 1 bar are 35.9 and 20.9 $cm^3\ g^{-1}$ for CH_4, 65.9 and 50.6 $cm^3\ g^{-1}$ for C_2H_6, 67.7 and 54.7 $cm^3\ g^{-1}$ for C_2H_4, 88.3 and 75.1 $cm^3\ g^{-1}$ for C_2H_2, 60.3 and 47.7 $cm^3\ g^{-1}$ for C_3H_8, and 67.0 and 58.5 $cm^3\ g^{-1}$ for C_3H_6, respectively. It should be noted that, in the actual separation process, the role of the volumetric storage capacity is also a significant criterion than the corresponding gravimetric capacity because it can take full advantage of the space of the separation unit and decrease the equipment cost. Accordingly, under ambient conditions (298 K and 1 bar), the calculated volumetric adsorption capacity of **NUM-18a** for C2–C3 hydrocarbons are 73.0 $cm^3\ cm^{-3}$ (C_2H_6), 79.0 $cm^3\ cm^{-3}$ (C_2H_4), 108.7 $cm^3\ cm^{-3}$ (C_2H_2), 68.9 $cm^3\ cm^{-3}$ (C_3H_8), and 84.4 $cm^3\ cm^{-3}$ (C_3H_6), respectively. Comparing the adsorption capacities of **NUM-18a** for single-component C1-C3 hydrocarbons gases, it can be seen that only a slight amount of CH_4 was adsorbed by **NUM-18a** at both two temperatures in the full range of pressure, which are obviously low to C2/C3 light hydrocarbons (Figs. S11-S14). It is worth mentioning that the most conspicuous differences in adsorption capacity between CH_4 and C2 hydrocarbons happen in the low-pressure region (<0.5 bar) of the isotherms, and the C_3H_8 and C_3H_6 in **NUM-18a** are also more rapidly approaching to saturation over CH_4 at lower pressure (<0.1 bar). The C_3H_8 uptake of 37.2 and 40.3 $cm^3\ g^{-1}$ at 0.1 bar is equal to over 78 and 90 % of the total uptake of 1 bar at 298 K. The low adsorption capacity of CH_4 should be related to the weak guest–host interactions between gas molecules and the MOF framework. The magnitude of the adsorption enthalpies reveals the affinity of the pore surface toward adsorbates, which plays a significant part in determining the adsorptive selectivity. To evaluate the affinity of such light hydrocarbons with the host framework, the coverage-dependent adsorption enthalpies (Q_{st}) of **NUM-18a** were calculated. The dual sites Langmuir-Freundlich equation was firstly used to fit the experimental unary isotherms of C1-C3 at 273 and 298 K, and the obtained fitting results are extremely matching well with the measured adsorption date (Table S2 and Fig. S15). The detail of the analytic procedure used is described in the supplementary information. The calculated Q_{st} ranges for CH_4, C_2H_6, C_2H_4, C_2H_2, C_3H_8, and C_3H_6 are in 26.0–26.0 kJ mol^{-1}, 35.3–40.4 kJ

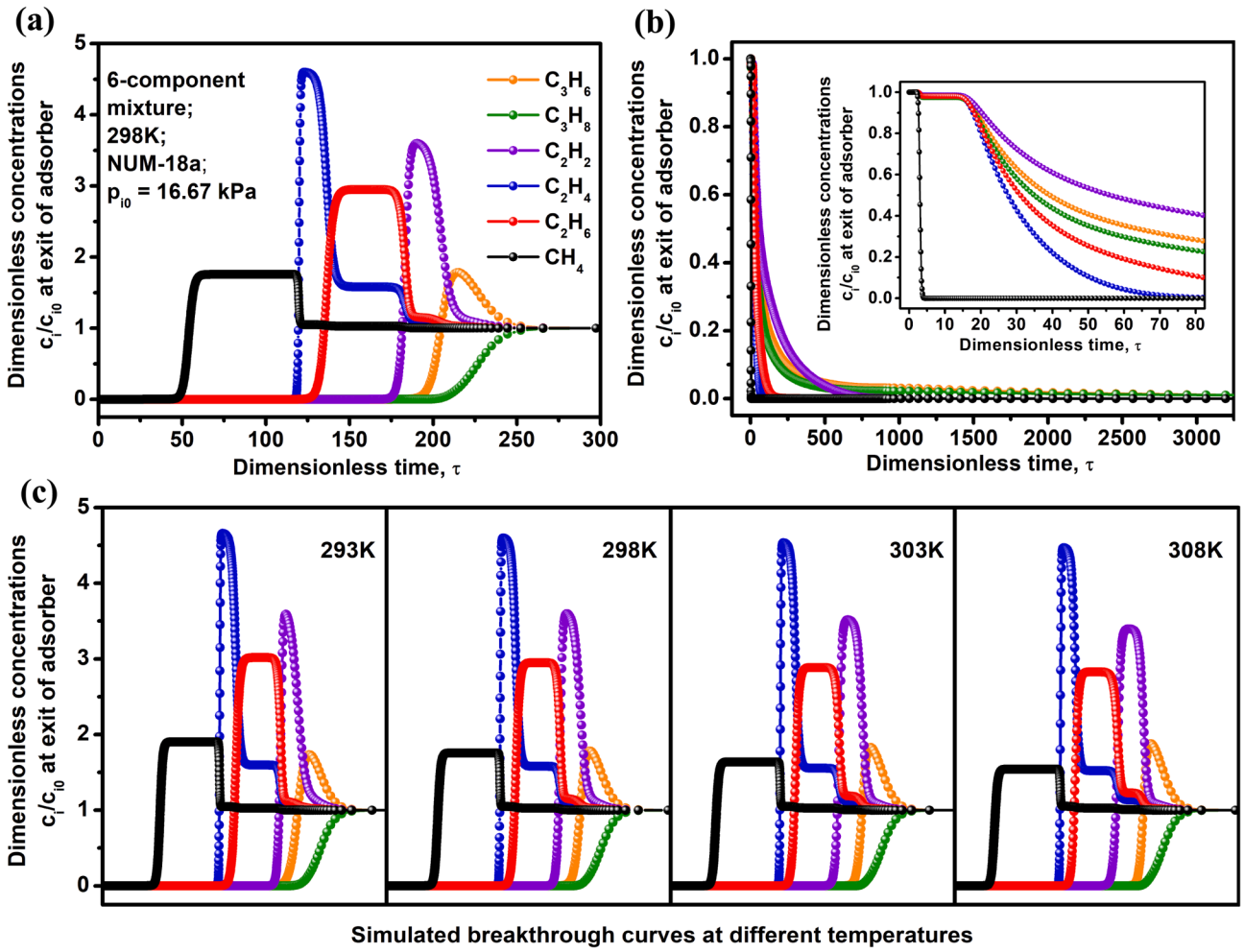

Fig. 5. (a) The simulated transient breakthrough curves of an equimolar 6-component mixture containing CH_4, C_2H_6, C_2H_4, C_2H_2, C_3H_8, and C_3H_6 in an adsorber packed with **NUM-18a**, operating under isothermal conditions at 298 K. The inlet gas was maintained at partial pressures P_{i0} = 16.67 kPa. (b) The simulated regeneration process of **NUM-18a** with He purge at 298 K and 100 kPa. (c) The simulated transient breakthrough curves at different temperatures. In (b) and (c), the symbol colors have the same meanings as (a).

mol^{-1}, 34.7–30.7 kJ mol^{-1}, 39.1–41.7 kJ mol^{-1}, 47.7–50.6 kJ mol^{-1} and 46.0–30.4 kJ mol^{-1}, respectively (Fig. 3d). Obviously, the resultant Q_{st} relationship at zero coverage is C_3H_8 (47.7 kJ mol^{-1}) > C_3H_6 (46.0 kJ mol^{-1}) > C_2H_2 (39.1 kJ mol^{-1}) > C_2H_6 (35.3 kJ mol^{-1}) > C_2H_4 (34.7 kJ mol^{-1}) > CH_4 (26.0 kJ mol^{-1}), which is indeed in good agreement with the adsorption phenomenon previously seen. The higher Q_{st} values of C2-C3 light hydrocarbons than that of CH_4 suggest **NUM-18a** may provide stronger affinities with these gases, which will result in them being preferentially adsorbed by **NUM-18a**.

3.4. Gas separation properties of NUM-18a

The considerable differences in uptake capacity and adsorption enthalpies of both C2-C3 hydrocarbons over CH_4 in **NUM-18a** encourage us further investigate its feasibility for CH_4 purification from 6-component C1/C2/C3 gas mixtures. The loading capacity of equimolar 6-component $CH_4/C_2H_6/C_2H_4/C_2H_2/C_3H_8/C_3H_6$ gas mixture, and adsorption selectivities of C_2H_6/CH_4, C_2H_4/CH_4, C_2H_2/CH_4, C_3H_8/CH_4, and C_3H_6/CH_4 were calculated by ideal adsorbed solution theory (IAST) to predict separating property of **NUM-18a** (Fig. 4a, b) [49]. The component loading curves indicate that the longer chain of the light hydrocarbon, the stronger adsorbability in **NUM-18a**, and the C_3H_8 has the highest component loading. Following the component loadings, we obtained the selectivity values for five equimolar binary pairs at 298 K and 100 kPa: 19.7 for C_2H_6/CH_4, 14.7 for C_2H_4/CH_4, 58.5 for C_2H_2/CH_4, 109.0 for C_3H_8/CH_4, and 86.9 for C_3H_6/CH_4. In its entirety, the selectivities of C2 and C3 components concerning CH_4 are in high excess of 10 and 80 for a region of pressures from 0 to 100 kPa. Among binary C2/CH_4 selectivities, the value of C_2H_2/CH_4 is most prominent, which outstrips many previously reported MOFs (such as FJU-36a [50], NKM-101a [51], ZJNU-98 [52], and FJI-C4 [53]) (Fig. 4c, and Table S3). The calculated C_3H_8/CH_4 selectivity is the highest in all binary (C2/C3)/CH_4 mixtures and is better than corresponding values of JLU-Liu34 [54], USTA-35a [55], MFM-202a [56], InOF-1 [57], and a large amount of other famous MOFs (Fig. 4d, and Table S4). These results further proved that **NUM-18a** is capable of high-selective separation of CH_4 from this complicated 6-components mixture.

To further demonstrate the potential of **NUM-18a** for CH_4 purification from gas mixtures containing C1-C3 hydrocarbons, transient breakthrough simulations were carried out. Assuming the adsorber filled with **NUM-18a** was maintained at an isotherm condition of 298 K with a total pressure of 100 kPa at the inlet, the transient breakthrough experiment of equimolar 6-component $CH_4/C_2H_6/C_2H_4/C_2H_2/C_3H_8/C_3H_6$ mixtures with partial pressures of 16.67 kPa for each component was determined. From the breakthrough curves in Fig. 5a, it can be observed that CH_4 gas as the effluent earliest flows out of the adsorber due to the most inferior adsorption strength when the mixed gas is passed through the packed column. Subsequently, the breakthrough of C2 and C3 components gradually happens with a sequential hierarchy of C_2H_4, C_2H_6, C_2H_2, C_3H_6, and C_3H_8. It is worth noting that there is a very

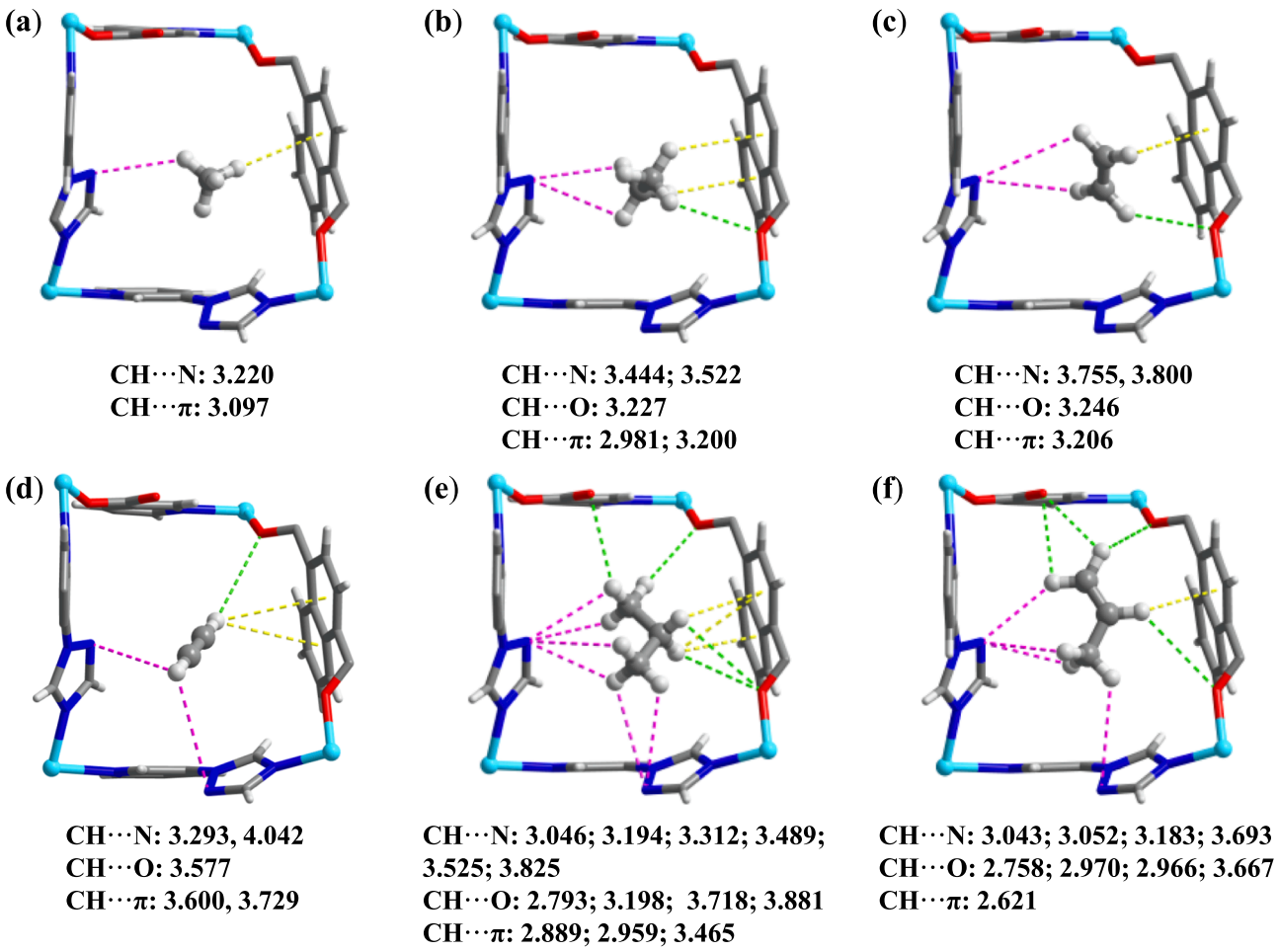

Fig. 6. The GCMC calculated adsorption sites of CH_4 (a), C_2H_6 (b), C_2H_4 (c), C_2H_2 (d), C_3H_8 (e), and C_3H_6 (f) in **NUM-18a** at 298 K and 1 bar (The unit of interaction distances is Å).

significant time interval between the breakthrough of CH_4 and C2/C3 hydrocarbons which is highly desirable because this means longer cycle times before the adsorbing column has to be regenerated. Concurrently, the regeneration of materials is also a very important procedure for gas separation in practical applications. We performed desorption simulations after finishing once breakthrough adsorption, in which the component loadings equilibrated bed is purged by the introduction of an inert (non-adsorbing gas) such as He at a total pressure of 100 kPa and 298 K. We note that the elution sequence of adsorbates is the same as aforementioned breakthrough order and the adsorbent can be regenerated after some time (Fig. 5b and S16). The sweeping recovery of C2-C3 hydrocarbons containing a very small amount of CH_4 can be achieved in desorption cycle. Furthermore, considering the exothermic nature of the adsorption phenomena that will result in significant temperature changes and further affect the adsorption of the mixtures, modeling the non-isothermal breakthrough characteristics is very necessary for understanding the influence of liberated heat in practical separation applications. However, it would require detailed information on (a) thermal heat capacity of fixed bed, (b) axial and radial dispersion characteristics, and (c) thermal conductivity of the bed of particles. There are sparse data on these parameters in the literature for MOFs. Therefore, we attempt to investigate the impact on separation performance by temperature change induced by adsorption in a different manner. We systematically carried out isothermal transient breakthrough simulations at a wide temperature range (293 K, 298 K, 303 K, and 308 K) to gain insights into the separation performances of at various temperatures. As shown in Fig. 5c and S17, the sequence of breakthrough of 6-component C1/C2/C3 mixtures remains unchanged at different temperatures and the dimensionless breakthrough times occur progressively earlier with increasing temperatures, as should be expected. Anyhow, the differences in breakthrough times between successive components are essentially unaltered. To some extent, this signifies that the separation performance seems to be not adversely influenced by temperature increases, and the separations with **NUM-18a** maybe are robust to temperature changes. However, although we respectively conducted a series of breakthrough simulations at different constant temperatures, the actual separation scenarios are generally non-isothermal conditions, and released adsorption heat will still influence the separation performance of **NUM-18a** to some extent. Overall, all of these breakthrough calculations undoubtedly attested to the potential of **NUM-18a** in purifying CH_4 from mixtures containing one or more of the C2-C3 impurity species.

3.5. GCMC simulations

To comprehensively and thoroughly explore the sorption mechanism of adsorbed guest C1-C3 hydrocarbon molecules in **NUM-18a**, the grand canonical Monte Carlo (GCMC) simulations had been carried out at 298 K and 1 bar. As shown in Fig. 6, we select three types of main interactions between gas molecules and pore walls to explain their adsorption behavior in **NUM-18a**, which are –CH···N hydrogen bond interaction induced by exposed N atoms, –CH···O hydrogen bond interaction from oxygen atoms of ligands, and –CH···π interaction within naphthalene rings. As for the whole structure, the CH_4 molecule only prefers to interact with one aromatic ring (3.097 Å) and a bare N atom (3.220 Å). The C_2H_6 molecule has two –CH···N interactions

(3.444–3.522 Å), one –CH···O (3.227 Å) interactions, and two –CH···π interaction (2.981–3.200 Å). The same applies to C_2H_2, however, the distances of two –CH···N interactions (3.293–4.042 Å) are shorter. The distances of –CH···O (3.577 Å) interaction and –CH···π interactions (3.600–3.729 Å) are longer at the same time. For C_2H_4, there are two –CH···N interactions (3.755–3.80 Å), one –CH···O (3.246 Å) interactions, and one –CH···π interaction (3.209 Å). Compared with C1-C2 hydrocarbons, more numerous interactions between C3 hydrocarbons and the host framework were found, which facilitate the formation of stronger affinities. As displayed in Fig. 6e, for C_3H_8, there are maximum adsorption sites, which are six –CH···N interactions (3.046–3.825 Å), four –CH···O (2.793–3.811 Å) interactions and three –CH···π interaction (2.889–3.465 Å). For C_3H_6, abundant sites are also discovered, that are four –CH···N interactions (3.043–3.693 Å), four –CH···O (2.758–3.667 Å) interactions and one –CH···π interaction (2.621 Å). Through GCMC calculations, it is found that **NUM-18** has the matched pore space and appropriate pore environment to form stronger affinities with C2-C3 hydrocarbon molecules than CH_4. Concurrently, these consequences from thermodynamics further prove the reliability of the experimental outcomes for adsorption and separation of such complex gases mixture.

4. Conclusion

In summary, we synthesized a robust 3D ultramicroporous MOF (**NUM-18**) by elaborately employing triangle and linear ligands, which feature fascinating 1D channels composed of two types of octahedral-like cages. The gas adsorption properties for C1-C3 light hydrocarbons of **NUM-18a** were systematically studied and the results indicate that **NUM-18a** has more distinguished C2-C3 hydrocarbons uptakes than CH_4. It is worth noting that **NUM-18a** can realize the highly selective separation of intimidating 6-component C1/C2/C3 mixtures as demonstrated by IAST calculations and transient breakthrough simulation. Moreover, the GCMC simulations provide a deep understanding of this excellent CH_4 separation performance of **NUM-18a**. All results of the experiments and calculations display that **NUM-18a** can efficiently purify CH_4 and recover C2-C3 hydrocarbons from C1/C2/C3 mixtures, as a promising porous adsorbent rivaling the top-performing MOFs. This work will offer tremendous encouragement for initiating more investigations on the emerging MOFs for such an industrially important separation.

CRediT authorship contribution statement

Qiang Zhang: Conceptualization, Methodology, Visualization, Investigation, Writing - original draft. **Xin Lian:** Software, Formal analysis, Visualization. **Rajamani Krishna:** Formal analysis, Methodology. **Shan-Qing Yang:** Investigation. **Tong-Liang Hu:** Supervision, Conceptualization, Project administration, Funding acquisition, Resources, Writing - review & editing.

Declaration of Competing Interest

The authors declare that they have no known competing financial interests or personal relationships that could have appeared to influence the work reported in this paper.

Data availability

No data was used for the research described in the article.

Acknowledgements

The authors acknowledge the Natural Science Foundation of Tianjin (20JCYBJC01330), and the National Natural Science Foundation of China (21673120) for financial support of this work.

Appendix A. Supplementary data

Supplementary data to this article can be found online at https://doi.org/10.1016/j.seppur.2022.122312.

References

[1] S. Zhou, O. Shekhah, A. Ramírez, P. Lyu, E. Abou-Hamad, J. Jia, J. Li, P.M. Bhatt, Z. Huang, H. Jiang, T. Jin, G. Maurin, J. Gascon, M. Eddaoudi, Asymmetric pore windows in MOF membranes for natural gas valorization, Nature 606 (7915) (2022) 706–712.
[2] Y. Belmabkhout, P.M. Bhatt, K. Adil, R.S. Pillai, A. Cadiau, A. Shkurenko, G. Maurin, G. Liu, W.J. Koros, M. Eddaoudi, Natural gas upgrading using a fluorinated MOF with tuned H_2S and CO_2 adsorption selectivity, Nat. Energy 3 (12) (2018) 1059–1066.
[3] W.-G. Cui, T.-L. Hu, X.-H. Bu, Metal-organic framework materials for the separation and purification of light hydrocarbons, Adv. Mater. 32 (3) (2020) 1806445.
[4] H. Zhang, P. Deria, O.K. Farha, J.T. Hupp, R.Q. Snurr, A thermodynamic tank model for studying the effect of higher hydrocarbons on natural gas storage in metal-organic frameworks, Energy Environ. Sci. 8 (5) (2015) 1501–1510.
[5] Y.-B. Wang, X.-Y. Li, X.-F. Du, C. He, C. Zhao, W. Yang, Efficient CH_4 separation and vapor uptakes in a porous MOF featuring 2D interlaced channels: experiment and simulation exploration, Sep. Purif. Technol. 298 (2022), 124645.
[6] D. Saha, H.A. Grappe, A. Chakraborty, G. Orkoulas, Postextraction separation, on-board storage, and catalytic conversion of methane in natural gas: A review, Chem. Rev. 116 (19) (2016) 11436–11499.
[7] S.-Q. Yang, T.-L. Hu, Reverse-selective metal-organic framework materials for the efficient separation and purification of light hydrocarbons, Coord. Chem. Rev. 468 (2022), 214628.
[8] R. Sahoo, M.C. Das, C2s/C1 hydrocarbon separation: The major step towards natural gas purification by metal-organic frameworks (MOFs), Coord. Chem. Rev. 442 (2021), 213998.
[9] O.T. Qazvini, R. Babarao, S.G. Telfer, Selective capture of carbon dioxide from hydrocarbons using a metal-organic framework, Nat. Commun. 12 (1) (2021) 197.
[10] J. Yang, J. Li, W. Wang, L. Li, J. Li, Adsorption of CO_2, CH_4, and N_2 on 8-, 10-, and 12-membered ring hydrophobic microporous high-silica zeolites: DDR, Silicalite-1, and Beta, Ind. Eng. Chem. Res. 52 (50) (2013) 17856–17864.
[11] X. Gao, Z. Li, C. Chen, C. Da, L. Liu, S. Tian, G. Ji, The determination of pore shape and interfacial barrier of entry for light gases transport in amorphous TEOS-derived silica: A finite element method, ACS Appl. Mater. Interfaces 13 (3) (2021) 4804–4812.
[12] S.-Q. Yang, F.-Z. Sun, R. Krishna, Q. Zhang, L. Zhou, Y.-H. Zhang, T.-L. Hu, Propane-trapping ultramicroporous metal-organic framework in the low-pressure area toward the purification of propylene, ACS Appl. Mater. Interfaces 13 (30) (2021) 35990–35996.
[13] W.-G. Cui, T.-L. Hu, Incorporation of active metal species in crystalline porous materials for highly efficient synergetic catalysis, Small 17 (22) (2021) 2003971.
[14] Y.-R. Zhang, X.-Z. Xie, X.-B. Yin, Y. Xia, Flexible ligand for metal-organic frameworks with simultaneous large-pore and antenna effect emission, Chem. Eng. J. 443 (2022), 136532.
[15] I. Abánades Lázaro, R.S. Forgan, Application of zirconium MOFs in drug delivery and biomedicine, Coord. Chem. Rev. 380 (2019) 230–259.
[16] H. Daglar, H.C. Gulbalkan, G. Avci, G.O. Aksu, O.F. Altundal, C. Altintas, I. Erucar, S. Keskin, Effect of metal-organic framework (MOF) database selection on the assessment of gas storage and separation potentials of MOFs, Angew. Chem. Int. Ed. 60 (14) (2021) 7828–7837.
[17] P. Liu, Y. Wang, Y. Chen, J. Yang, X. Wang, L. Li, J. Li, Construction of saturated coordination titanium-based metal-organic framework for one-step C_2H_2/C_2H_6/C_2H_4 separation, Sep. Purif. Technol. 276 (2021), 119284.
[18] O.T. Qazvini, R. Babarao, Z.-L. Shi, Y.-B. Zhang, S.G. Telfer, A robust ethane-trapping metal-organic framework with a high capacity for ethylene purification, J. Am. Chem. Soc. 141 (12) (2019) 5014–5020.
[19] Y. Zhao, J. Wang, Z. Bao, H. Xing, Z. Zhang, B. Su, Q. Yang, Y. Yang, Q. Ren, Adsorption separation of acetylene and ethylene in a highly thermostable microporous metal-organic framework, Sep. Purif. Technol. 195 (2018) 238–243.
[20] B. Zheng, X. Luo, Z. Wang, S. Zhang, R. Yun, L. Huang, W. Zeng, W. Liu, An unprecedented water stable acylamide-functionalized metal-organic framework for highly efficient CH_4/CO_2 gas storage/separation and acid-base cooperative catalytic activity, Inorg. Chem. Front. 5 (9) (2018) 2355–2363.
[21] T.-L. Hu, Y. Tao, Z. Chang, X.-H. Bu, Zinc(II) complexes with a versatile multitopic tetrazolate-based ligand showing various structures: Impact of reaction conditions on the final product structures, Inorg. Chem. 50 (21) (2011) 10994–11003.
[22] K. Jiang, L. Zhang, T. Xia, Y. Yang, B. Li, Y. Cui, G. Qian, A water-stable fcu-MOF material with exposed amino groups for the multi-functional separation of small molecules, Sci. China Mater. 62 (9) (2019) 1315–1322.
[23] Y. Liu, Q. Xu, L. Chen, C. Song, Q. Yang, Z. Zhang, D. Lu, Y. Yang, Q. Ren, Z. Bao, Hydrogen-bonded metal-nucleobase frameworks for highly selective capture of ethane/propane from methane and methane/nitrogen separation, Nano Res. (2022), https://doi.org/10.1007/s12274-022-4352-0.
[24] G.-D. Wang, H.-H. Wang, W.-J. Shi, L. Hou, Y.-Y. Wang, Z. Zhu, A highly stable MOF with F and N accessible sites for efficient capture and separation of acetylene from ternary mixtures, J. Mater. Chem. A 9 (43) (2021) 24495–24502.

[25] L. Meng, L. Yang, C. Chen, X. Dong, S. Ren, G. Li, Y. Li, Y. Han, Z. Shi, S. Feng, Selective acetylene adsorption within an imino-functionalized nanocage-based metal-organic framework, ACS Appl. Mater. Interfaces 12 (5) (2020) 5999–6006.
[26] Y. He, C. Song, Y. Ling, C. Wu, R. Krishna, B. Chen, A new MOF-5 homologue for selective separation of methane from C2 hydrocarbons at room temperature, APL Mater. 2 (12) (2014), 124102.
[27] X. Duan, Q. Zhang, J. Cai, Y. Yang, Y. Cui, Y. He, C. Wu, R. Krishna, B. Chen, G. Qian, A new metal-organic framework with potential for adsorptive separation of methane from carbon dioxide, acetylene, ethylene, and ethane established by simulated breakthrough experiments, J. Mater. Chem. A 2 (8) (2014) 2628–2633.
[28] Y. He, W. Zhou, R. Krishna, B. Chen, Microporous metal-organic frameworks for storage and separation of small hydrocarbons, Chem. Commun. 48 (97) (2012) 11813–11831.
[29] A.M. Plonka, X. Chen, H. Wang, R. Krishna, X. Dong, D. Banerjee, W.R. Woerner, Y. Han, J. Li, J.B. Parise, Light hydrocarbon adsorption mechanisms in two calcium-based microporous metal organic frameworks, Chem. Mater. 28 (6) (2016) 1636–1646.
[30] L. Li, R. Krishna, Y. Wang, J. Yang, X. Wang, J. Li, Exploiting the gate opening effect in a flexible MOF for selective adsorption of propyne from C1/C2/C3 hydrocarbons, J. Mater. Chem. A 4 (3) (2016) 751–755.
[31] R.-B. Lin, Z. Zhang, B. Chen, Achieving high performance metal-organic framework materials through pore engineering, Acc. Chem. Res. 54 (17) (2021) 3362–3376.
[32] H. Wang, Y. Liu, J. Li, Designer metal-organic frameworks for size-exclusion-based hydrocarbon separations: Progress and challenges, Adv. Mater. 32 (44) (2020) 2002603.
[33] D.-W. Lim, J. Ha, Y. Oruganti, H.R. Moon, Hydrogen separation and purification with MOF-based materials, Mater. Chem. Front. 5 (11) (2021) 4022–4041.
[34] A. Pal, S. Chand, D.G. Madden, D. Franz, L. Ritter, B. Space, T. Curtin, S. Chand Pal, M.C. Das, Immobilization of a polar sulfone moiety onto the pore surface of a humid-stable MOF for highly efficient CO_2 separation under dry and wet environments through direct CO_2-sulfone interactions, ACS Appl. Mater. Interfaces 12 (37) (2020) 41177–41184.
[35] Y.-Z. Li, G.-D. Wang, W.-J. Shi, L. Hou, Y.-Y. Wang, Z. Zhu, Efficient $C2H_n$ hydrocarbons and VOC adsorption and separation in an MOF with lewis basic and acidic decorated active sites, ACS Appl. Mater. Interfaces 12 (37) (2020) 41785–41793.
[36] X. Han, X. Yang, C. Yu, S. Lu, E.S. Pouya, P. Bai, J. Lyu, X. Guo, Fine-tuning the pore structure of metal-organic frameworks by linker substitution for enhanced hydrogen storage and gas separation, CrystEngComm 23 (16) (2021) 3026–3032.
[37] T.-L. Hu, H. Wang, B. Li, R. Krishna, H. Wu, W. Zhou, Y. Zhao, Y. Han, X. Wang, W. Zhu, Z. Yao, S. Xiang, B. Chen, Microporous metal-organic framework with dual functionalities for highly efficient removal of acetylene from ethylene/acetylene mixtures, Nat. Commun. 6 (1) (2015) 7328.
[38] Y. Ye, Z. Ma, R.-B. Lin, R. Krishna, W. Zhou, Q. Lin, Z. Zhang, S. Xiang, B. Chen, Pore space partition within a metal-organic framework for highly efficient C_2H_2/CO_2 separation, J. Am. Chem. Soc. 141 (9) (2019) 4130–4136.
[39] H. Li, L. Li, R.-B. Lin, G. Ramirez, W. Zhou, R. Krishna, Z. Zhang, S. Xiang, B. Chen, Microporous metal-organic framework with dual functionalities for efficient separation of acetylene from light hydrocarbon mixtures, ACS Sustainable Chem. Eng. 7 (5) (2019) 4897–4902.
[40] B. Li, D. Ma, Y. Li, Y. Zhang, G. Li, Z. Shi, S. Feng, M.J. Zaworotko, S. Ma, Dual functionalized cages in metal-organic frameworks via stepwise postsynthetic modification, Chem. Mater. 28 (13) (2016) 4781–4786.
[41] W.-Q. Lin, X.-L. Xiong, H. Liang, G.-H. Chen, Multiscale computational screening of metal-organic frameworks for Kr/Xe adsorption separation: a structure-property relationship-based screening strategy, ACS Appl. Mater. Interfaces 28 (13) (2021) 17998–18009.
[42] W. Gong, Y. Xie, T.D. Pham, S. Shetty, F.A. Son, K.B. Idrees, Z. Chen, H. Xie, Y. Liu, R.Q. Snurr, B. Chen, B. Alameddine, Y. Cui, O.K. Farha, Creating optimal pockets in a clathrochelate-based metal-organic framework for gas adsorption and separation: experimental and computational studies, J. Am. Chem. Soc. 144 (8) (2022) 3737–3745.
[43] M.-H. Yu, P. Zhang, R. Feng, Z.-Q. Yao, Y.-C. Yu, T.-L. Hu, X.-H. Bu, Construction of a multi-cage-based MOF with a unique network for efficient CO_2 capture, ACS Appl. Mater. Interfaces 9 (31) (2017) 26177–26183.
[44] Q. Zhang, S.-Q. Yang, L. Zhou, L. Yu, Z.-F. Li, Y.-J. Zhai, T.-L. Hu, Pore-space partition through an embedding metal-carboxylate chain-induced topology upgrade strategy for the separation of acetylene/ethylene, Inorg. Chem. 60 (24) (2021) 19328–19335.
[45] Q. Zhang, L. Zhou, P. Liu, L. Li, S.-Q. Yang, Z.-F. Li, T.-L. Hu, Integrating tri-mural nanotraps into a microporous metal-organic framework for C_2H_2/CO_2 and C_2H_2/C_2H_4 separation, Sep. Purif. Technol. 296 (2022) 21404.
[46] G.M. Sheldrick, SHELXT - integrated space-group and crystal-structure determination, Acta Cryst. A 71 (1) (2015) 3–8.
[47] G.M. Sheldrick, Crystal structure refinement with SHELXL, Acta Cryst. C 71 (1) (2015) 3–8.
[48] A. Spek, Single-crystal structure validation with the program PLATON, J. Appl. Crystallogr. 36 (1) (2003) 7–13.
[49] A.L. Myers, J.M. Prausnitz, Thermodynamics of mixed-gas adsorption, AlChE J. 11 (1) (1965) 121–127.
[50] L. Liu, Z. Yao, Y. Ye, L. Chen, Q. Lin, Y. Yang, Z. Zhang, S. Xiang, Robustness, selective gas separation, and nitrobenzene sensing on two isomers of cadmium metal-organic frameworks containing various metal-O-metal chains, Inorg. Chem. 57 (20) (2018) 12961–12968.
[51] Y. Qiao, X. Chang, J. Zheng, M. Yi, Z. Chang, M.-H. Yu, X.-H. Bu, Self-interpenetrated water-stable microporous metal-organic framework toward storage and purification of light hydrocarbons, Inorg. Chem. 60 (4) (2021) 2749–2755.
[52] M. He, T. Xu, Z. Jiang, L. Yang, Y. Zou, F. Xia, X. Wang, X. Wang, Y. He, Incorporation of bifunctional aminopyridine into an NbO-type MOF for the markedly enhanced adsorption of CO_2 and C_2H_2 over CH_4, Inorg. Chem. Front. 6 (5) (2019) 1177–1183.
[53] L. Li, X. Wang, J. Liang, Y. Huang, H. Li, Z. Lin, R. Cao, Water-stable anionic metal-organic framework for highly selective separation of methane from natural gas and pyrolysis gas, ACS Appl. Mater. Interfaces 8 (15) (2016) 9777–9781.
[54] J. Zhang, S. Yao, S. Liu, B. Liu, X. Sun, B. Zheng, G. Li, Y. Li, Q. Huo, Y. Liu, Enhancement of gas sorption and separation performance via ligand functionalization within highly stable zirconium-based metal-organic frameworks, Cryst. Growth Des. 17 (4) (2017) 2131–2139.
[55] Y. He, Z. Zhang, S. Xiang, F.R. Fronczek, R. Krishna, B. Chen, A robust doubly interpenetrated metal-organic framework constructed from a novel aromatic tricarboxylate for highly selective separation of small hydrocarbons, Chem. Commun. 48 (52) (2012) 6493–6495.
[56] S. Gao, C.G. Morris, Z. Lu, Y. Yan, H.G.W. Godfrey, C. Murray, C.C. Tang, K. M. Thomas, S. Yang, M. Schröder, Selective hysteretic sorption of light hydrocarbons in a flexible metal-organic framework material, Chem. Mater. 28 (7) (2016) 2331–2340.
[57] Y. Chen, Z. Qiao, D. Lv, H. Wu, R. Shi, Q. Xia, H. Wang, J. Zhou, Z. Li, Selective adsorption of light alkanes on a highly robust indium based metal-organic framework, Ind. Eng. Chem. Res. 56 (15) (2017) 4488–4495.

Supporting Information

An ultramicroporous metal-organic framework based on octahedral-like cages showing high-selective methane purification from a six-component C1/C2/C3 hydrocarbons mixture

Qiang Zhang,[a] Xin Lian,[a] Rajamani Krishna,[b] Shan-Qing Yang,[a] and Tong-Liang Hu*,[a]

[a] School of Materials Science and Engineering, National Institute for Advanced Materials, Nankai University, Tianjin 300350, China.

[b] Van 't Hoff Institute for Molecular Sciences, University of Amsterdam, Science Park 904, 1098 XH Amsterdam, The Netherlands.

Email: tlhu@nankai.edu.cn (T.-L. Hu).

Table of contents

References

S1. Supplementary methods

1. Fitting of unary isotherm data

The unary isotherms for CH_4, C_2H_6, C_2H_4, C_2H_2, C_3H_8, and C_3H_6 measured at two different temperatures 273 K, and 298 K in **NUM-18a** were fitted with excellent accuracy using the dual-site Langmuir-Freundlich model, where we distinguish two distinct adsorption sites A and B:

$$q = \frac{q_{sat,A} b_A p^{vA}}{1 + b_A p^{vA}} + \frac{q_{sat,B} b_B p^{vB}}{1 + b_B p^{vB}} \qquad (S1)$$

In eq. (S1), the Langmuir-Freundlich parameters b_A and b_B are both temperature dependent:

$$b_A = b_{A0} \exp\left(\frac{E_A}{RT}\right);\ b_B = b_{B0} \exp\left(\frac{E_B}{RT}\right) \qquad (S2)$$

In eq (S2), E_A and E_B are the energy parameters associated with sites A, and B, respectively.

The unary isotherm fit parameters for each of the guest molecules in **NUM-18a** are provided in Table S2.

2. Isosteric heat of adsorption calculations

The isosteric heat of adsorption (Q_{st}) is defined as:

$$Q_{st} = -RT^2 \left(\frac{\partial ln p}{\partial T}\right) \qquad (S3)$$

Where the derivative in the right member of eq (S3) is determined at constant adsorbate loading, **q**; the derivative can be determined analytically using equations (S1), (S2), and (S3).

3. IAST calculations of selectivity

The adsorption selectivity for separation for components 1 and 2 is defined by:

$$S_{ads} = \frac{q_1/q_2}{p_1/p_2} \qquad (S4)$$

IAST calculations were carried out for equimolar $C_3H_6/C_3H_8/C_2H_2/C_2H_4/C_2H_6/CH_4$ mixtures at 298 K.

4. Breakthrough simulations

The performance of industrial fixed bed adsorbers is dictated by a combination of adsorption selectivity and uptake capacity. Transient breakthrough simulations were carried out for $C_3H_6/C_3H_8/C_2H_2/C_2H_4/C_2H_6/CH_4$ mixtures in a wide temperature range (293 K, 298 K, 303 K, 308 K, respectively) with partial pressures of 16.666 kPa for each component in a tube packed with **NUM-18a**, using the methodology described in earlier publications.[1-5] For the breakthrough simulations, the following parameter values were used: length of packed bed, L = 0.30 m; voidage of packed bed, ε = 0.40; superficial gas velocity at inlet, u = 0.04 m s^{-1}.

The *y*-axis is the dimensionless concentrations of each component at the exit of the fixed bed, normalized with respect to the inlet feed concentrations. The *x*-axis is the dimensionless time, $\tau = \frac{tu}{L\varepsilon}$, defined by dividing the actual time, *t*, by the characteristic time, $\frac{L\varepsilon}{u}$.

5. Grand Canonical Monte Carlo simulations

The Grand Canonical Monte Carlo simulations were performed for the adsorption of C1-C3 light hydrocarbons in **NUM-18a** with the Material Studio 8.0. The optimal adsorption sites were simulated under 298 K with a pressure of 1.0 bar. We used 1.0×10^7 cycles for equilibration and the production steps were set to 1.0×10^6. The framework of **NUM-18a** was treated as a rigid structure and so did the adsorbate molecules. A standard Lennard-Jones and Coulomb model was used and the Lennard-Jones parameters for the framework atoms as well as adsorbate molecules were adopted from the universal force field (UFF). Ewald summation was used to calculate electrostatic interactions for both adsorbent-adsorbate and adsorbate-adsorbate interactions.

Notation

b	Langmuir-Freundlich parameter, Pa^{-v}
E	energy parameter, J mol^{-1}
p	pressure, Pa
q	component molar loading of species i, mol kg^{-1}

q_{sat} saturation loading, mol kg^{-1}

L length of packed bed adsorber, m

t time, s

T absolute temperature, K

u superficial gas velocity in packed bed, m s^{-1}

Greek letters

v Freundlich exponent, dimensionless

ε voidage of packed bed, dimensionless

τ time, dimensionless

S2. Supplementary tables

Table S1. Crystal data and structure refinement parameters for **NUM-18**

Empirical formula	$C_{28}\ H_{18}\ Co_2\ N_8\ O_9$
Formula weight (g mol^{-1})	719.03
Crystal system	monoclinic
Space group	*C2/c*
a (Å)	21.5876(3)
b (Å)	12.4616(2)
c (Å)	14.4975(2)
β(°)	98.319(1)
V ($Å^3$)	3859.02(1)
Z	4
ρ_{calc} (g cm^{-3})	1.238
μ (mm^{-1})	7.192
F (000)	1452.0
2Θ range for data collection/°	8.214 to 151.842
Index ranges	-21≤h≤26, -15≤k≤7, -15≤l≤18
Reflections collected	9959
Independent reflections	3863 [R_{int} = 0.0192, R_{sigma} = 0.0229]
Goodness-of-fit on F^2	1.150
Final R indexes [I>=2σ (I)][a]	R_1 = 0.0582, wR_2 = 0.1589
Final R indexes [all data][b]	R_1 = 0.0592, wR_2 = 0.1593
Largest diff. peak/hole / e $Å^{-3}$	1.07/-0.68
CCDC deposition number	2113559

[a]$R_1=\sum||F_o|-|F_c||/\sum|F_o|$, [b]$wR_2=\{\sum[w(F_o^2-F_c^2)^2]/\sum w(F_o^2)^2\}^{1/2}$

Table S2. Dual-site Langmuir-Freundlich parameters for C1/C2/C3 in **NUM-18a**

	Site A				**Site B**			
	$q_{A,sat}$ mol kg^{-1}	b_{A0} Pa^{-vA}	E_A kJ mol^{-1}	*vA*	$q_{B,sat}$ mol kg^{-1}	b_{B0} Pa^{-vB}	E_B kJ mol^{-1}	*vB*
C_3H_6	1.1	4.105E-11	46.0	0.88	2.5	2.966E-06	16.7	0.55
C_3H_8	0.9	6.048E-13	56.0	1.20	2.1	1.070E-07	26.3	0.52
C_2H_2	2.7	2.647E-11	39.0	1.00	1.5	5.437E-13	42.0	1.00
C_2H_4	1.2	1.209E-10	35.3	1.00	2.2	5.614E-11	30.5	1.00
C_2H_6	1.1	4.139E-10	35.0	1.00	2.0	1.219E-12	40.5	1.00
CH_4	2.6	1.580E-10	26.0	1.00				

Table S3. Comparison of C_2H_2/CH_4 selectivities for **NUM-18a** and other MOFs

MOFs	Selectivity	Ref.
$Cu(SiF_6)(sdi)_2$	11.2	6
QMOF-1a	13.5	7
SNNU-5-Sc	13.5	8
SNNU-61	14.4	9
FJU-36a	17.7	10
JLU-Liu67	20.0	11
ZJU-15	22	12
UTSA-72	26.5	13
NKM-101a	28.7	14
ZJNU-98	30.5	15
$Ca(dtztp)_{0.5}$	33.3	16
Eu-BDC-NH_2	33.4	17
BSF-1	46.9	18
FJI-C4	51.0	19
NUM-18a	58.5	This work
BUT-70A	66.6	20
CuDTTA	166	21

Table S4. Comparison of C_3H_8/CH_4 selectivities for **NUM-18a** and other MOFs

MOFs	Selectivity	Ref.
JLU-Liu34	45.9	22
Zr-2,6-NDC	49.2	23
Zr-BPDC	65.0	23
JUC-100	65	24
JUC-103	65	24
JUC-106	65	24
Zr-BDC	71.5	23
Zr-1,4-NDC	73.5	23
FIR-51	75	25
FIR-7a-ht	78.8	26
UTSA-35a	85	27
MFM-202a	87	28
InOF-1	90	29
JLU-Liu5	107.8	30
NUM-18a	109.0	This work
JLU-Liu6	274.6	30
FJI-C4	293.4	19

S3. Supplementary figures

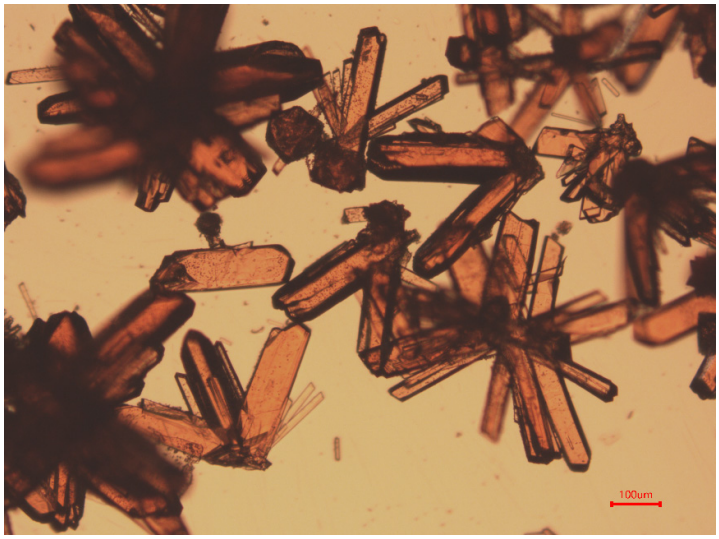

Figure S1. Optical microscope image of **NUM-18**.

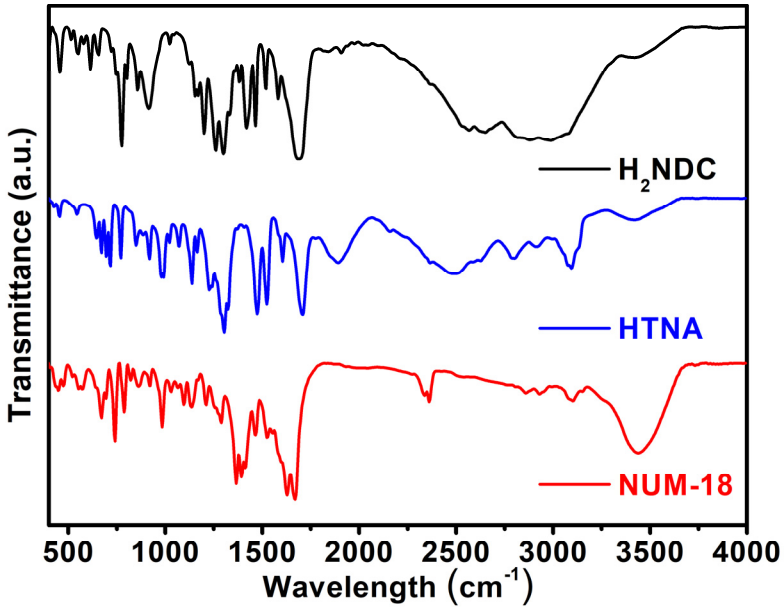

Figure S2. Comparison of FTIR spectra of as-synthesized **NUM-18** and ligands.

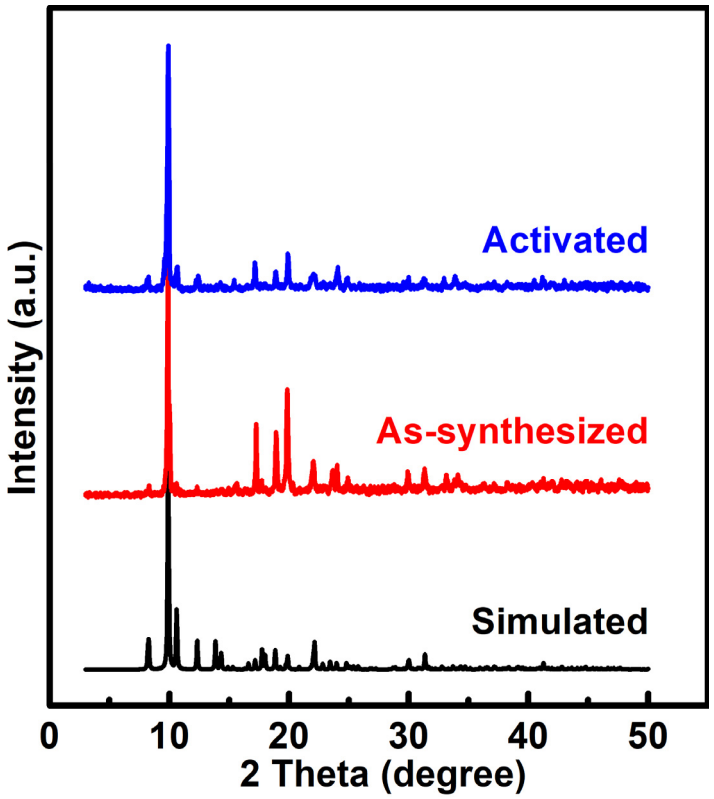

Figure S3. Comparison of simulated, experimental and activated PXRD patterns of **NUM-18**.

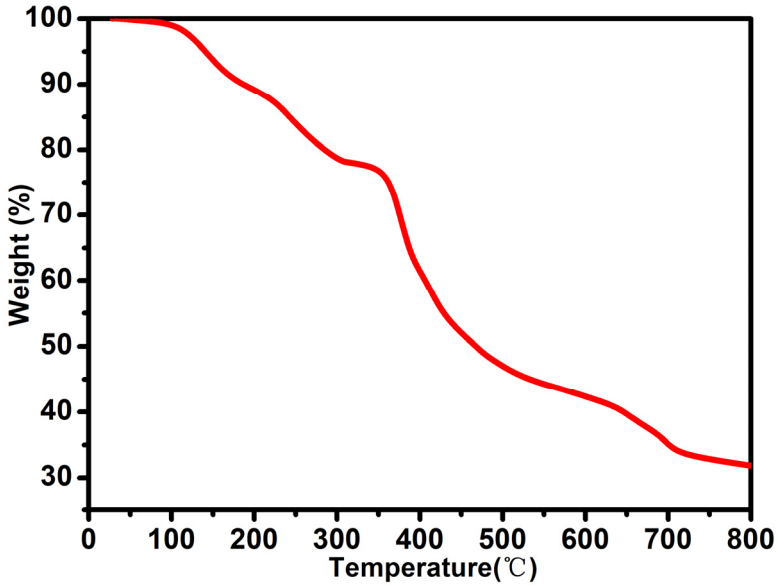

Figure S4. TGA curve for **NUM-18** under Ar atmosphere.

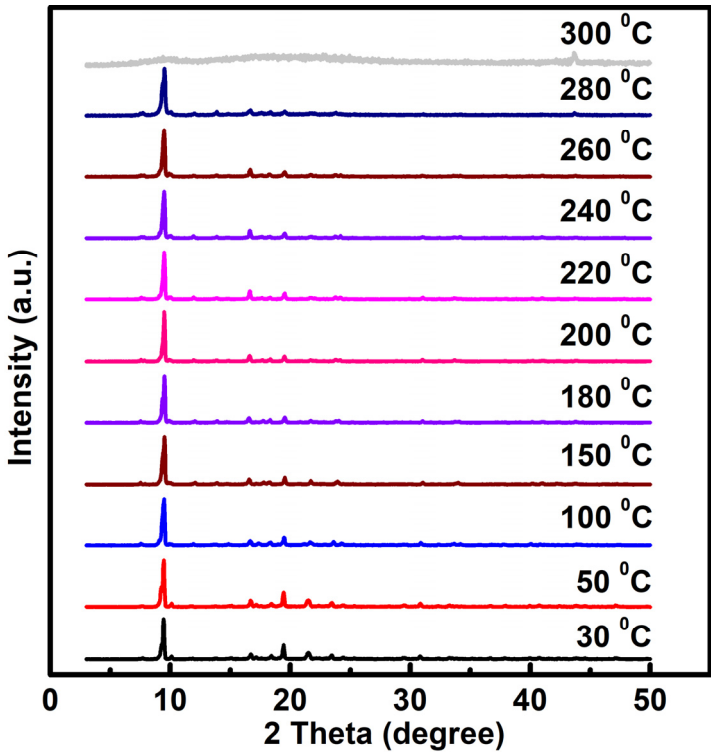

Figure S5. The VT-PXRD patterns of **NUM-18** under air atmosphere.

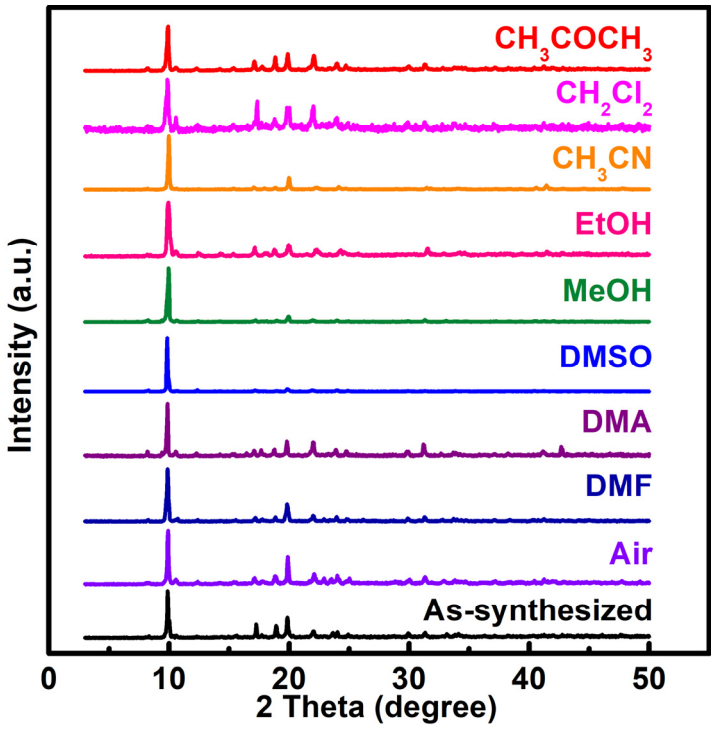

Figure S6. The PXRD patterns for **NUM-18** after exposed in air or immersed in common solvents a week.

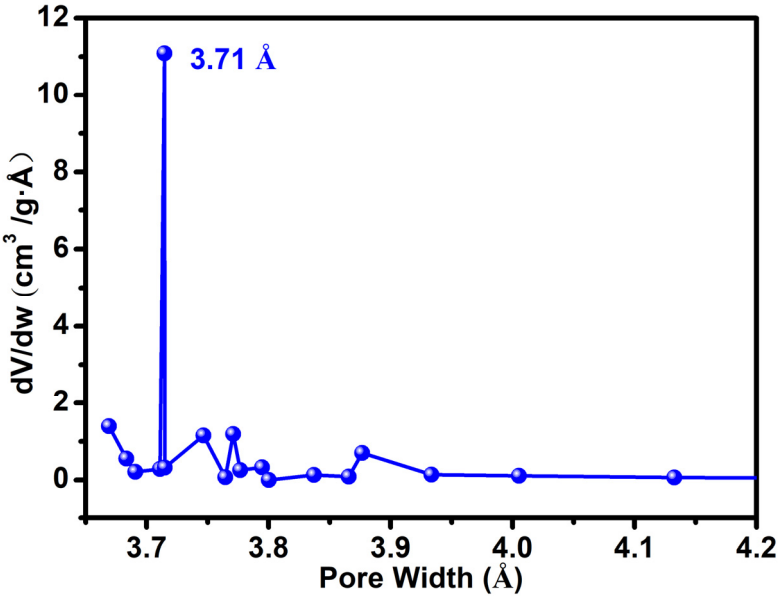

Figure S7. The pore size distribution of **NUM-18a**.

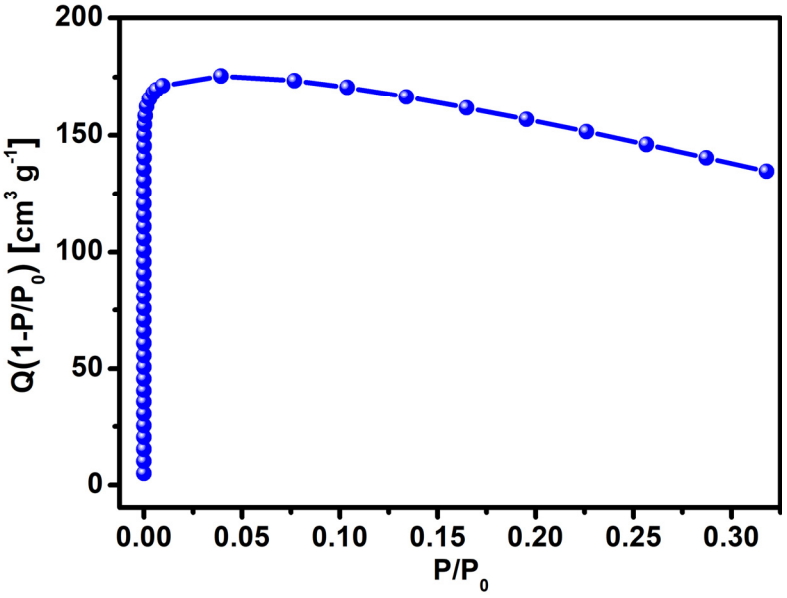

Figure S8. The plot of the term $Q(1-P/P_0)$ vs P/P_0 in **NUM-18a**.

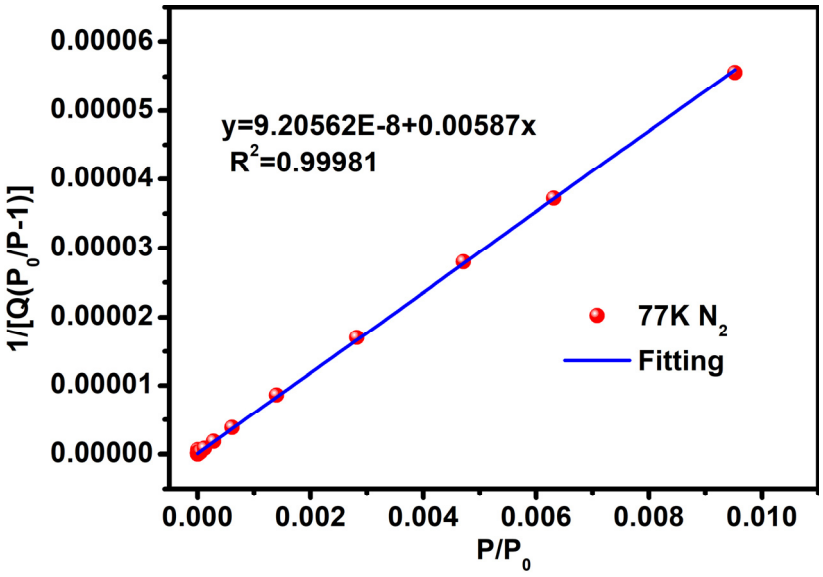

Figure S9. The consistency plot for BET surface areas fitting in **NUM-18a**.

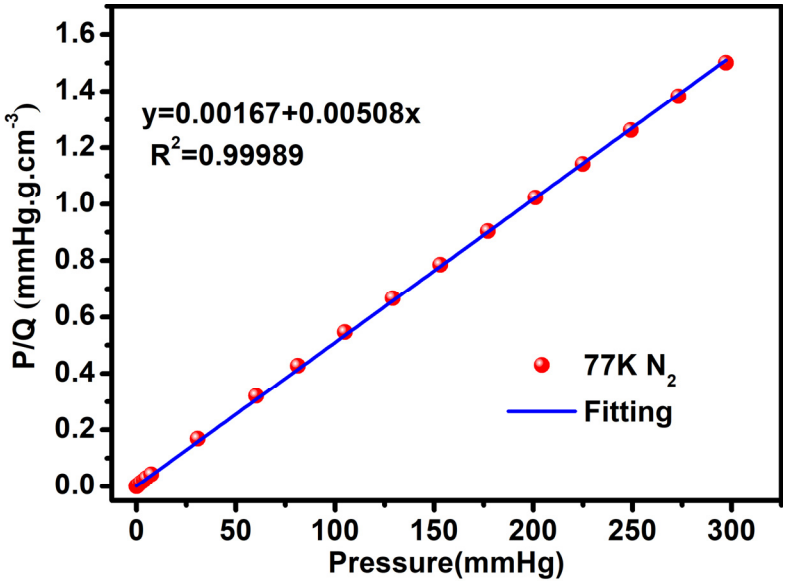

Figure S10. The consistency plot for Langmuir surface areas fitting in **NUM-18a**.

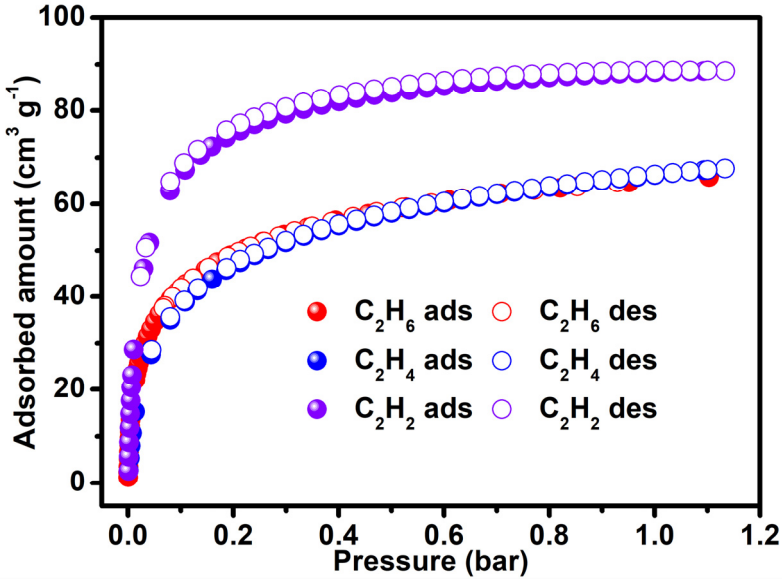

Figure S11. Gas sorption isotherms of **NUM-18a** for C_2H_6, C_2H_4, and C_2H_2 at 273K.

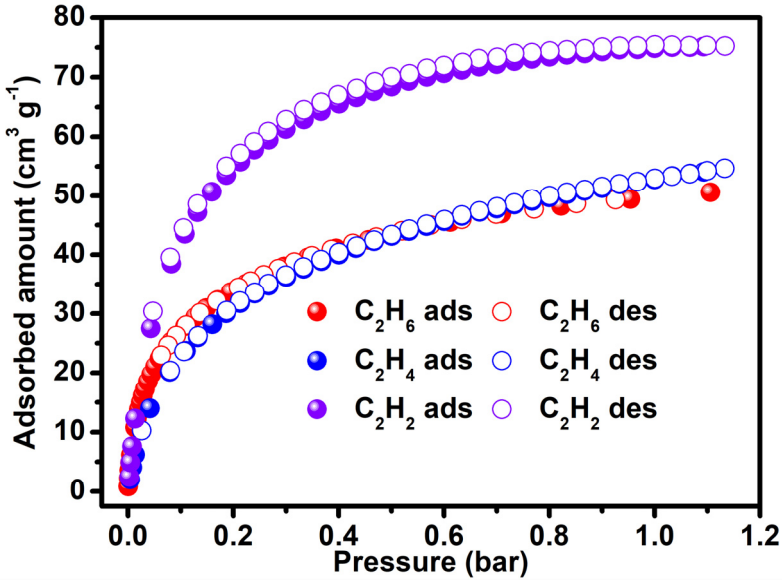

Figure S12. Gas sorption isotherms of **NUM-18a** for C_2H_6, C_2H_4, and C_2H_2 at 298K.

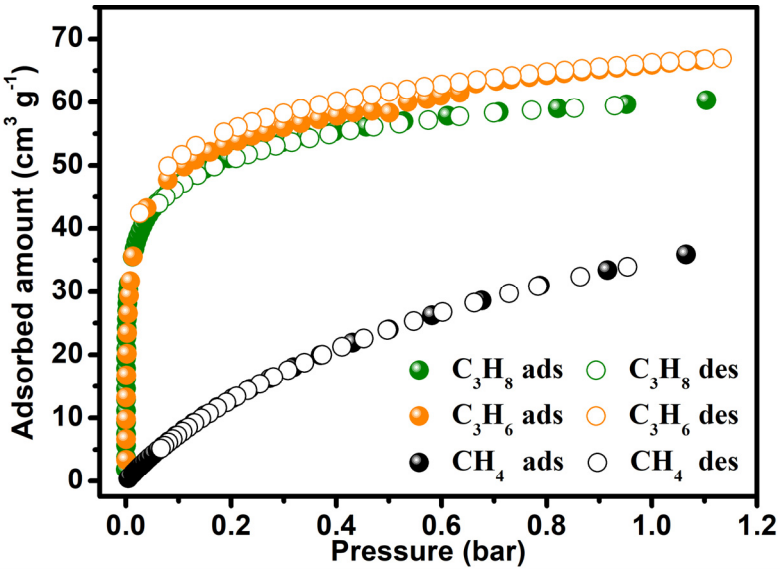

Figure S13. Gas sorption isotherms of **NUM-18a** for C_3H_8, C_3H_6 and CH_4 at 273K.

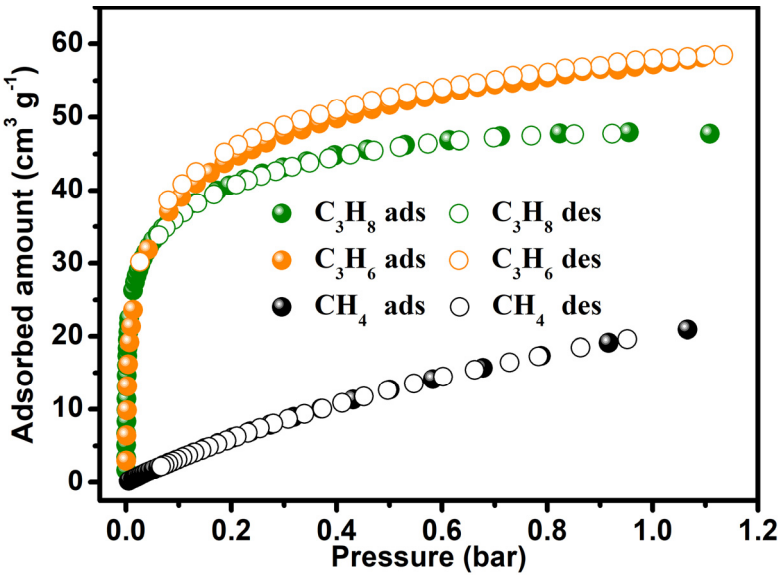

Figure S14. Gas sorption isotherms of **NUM-18a** for C_3H_8, C_3H_6 and CH_4 at 298K.

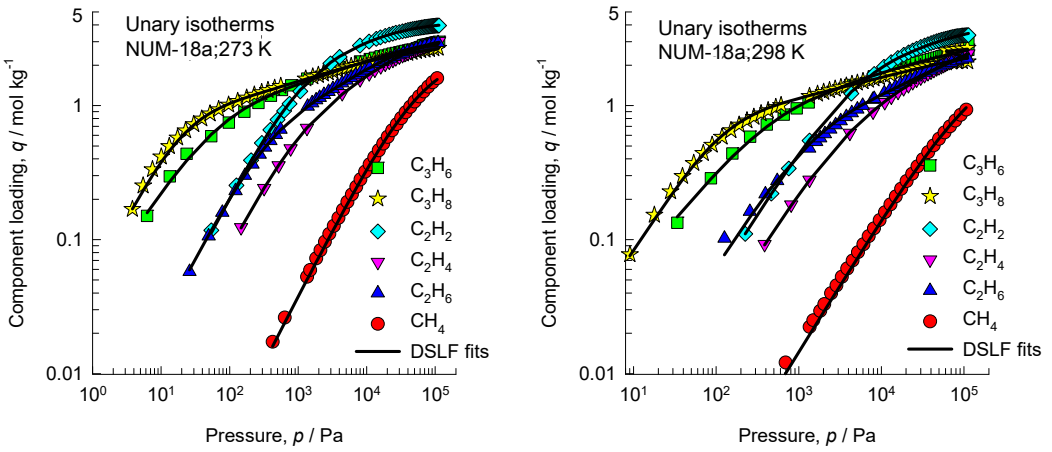

Figure S15. The details of dual-Langmuir-Freundlich isotherm (solid lines) fitting to the experimental C1-C3 hydrocarbon adsorption data (symbols) for **NUM-18a** at 273 and 298 K.

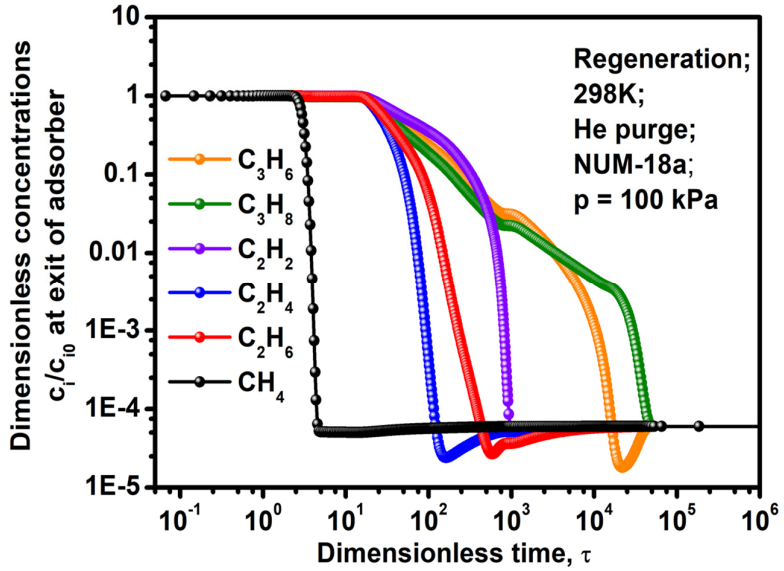

Figure S16. The simulated regeneration process of **NUM-18a** with He purge at 298 K and 100 kPa.

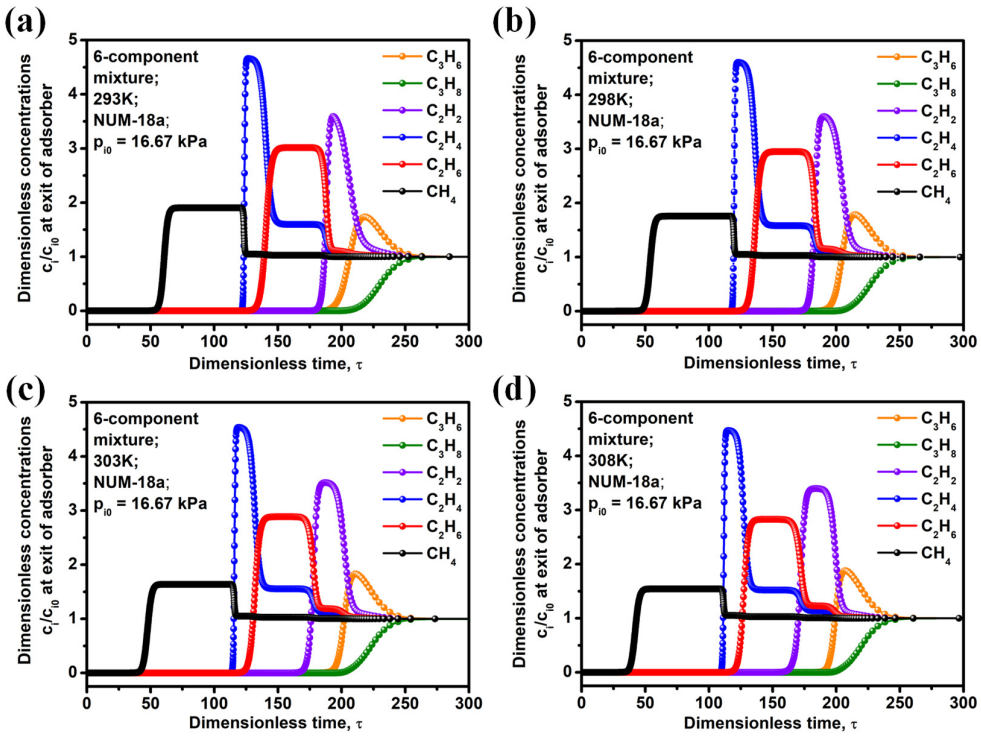

Figure S17. The simulated transient breakthrough curves of an equimolar 6-component mixture containing CH_4, C_2H_6, C_2H_4, C_2H_2, C_3H_8, and C_3H_6 in an adsorber packed with **NUM-18a**, operating under isothermal conditions at (a) 293 K, (b) 298 K, (c) 303 K, and (d) 308 K, respectively. The inlet gas is maintained at partial pressures P_{i0} = 16.67 kPa.

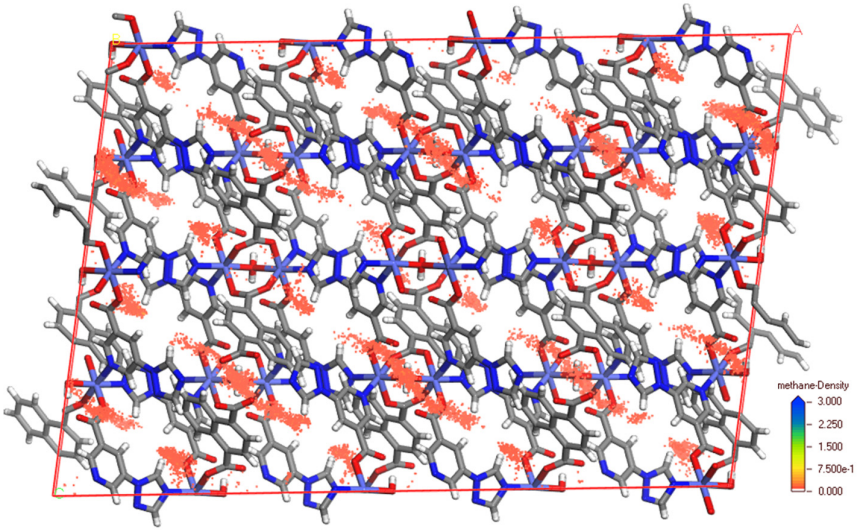

Figure S18. Density distribution of CH_4 in **NUM-18a** at 298 K and 1 bar.

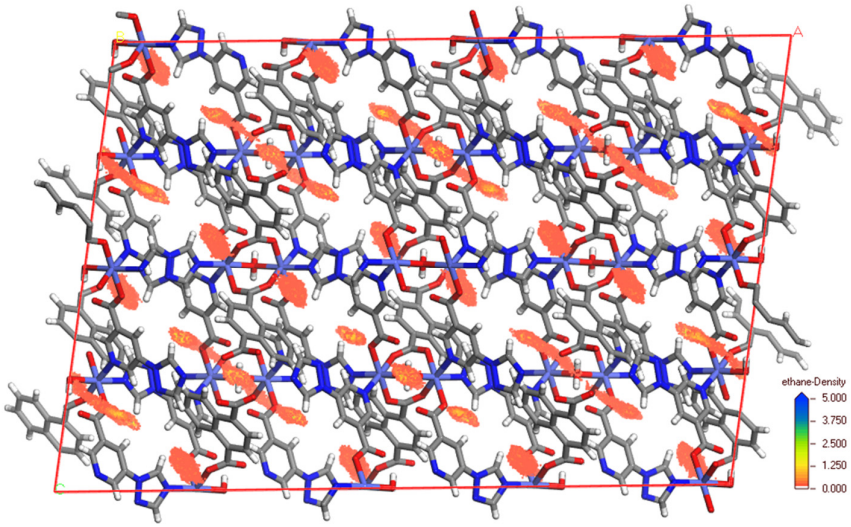

Figure S19. Density distribution of C_2H_6 in **NUM-18a** at 298 K and 1 bar.

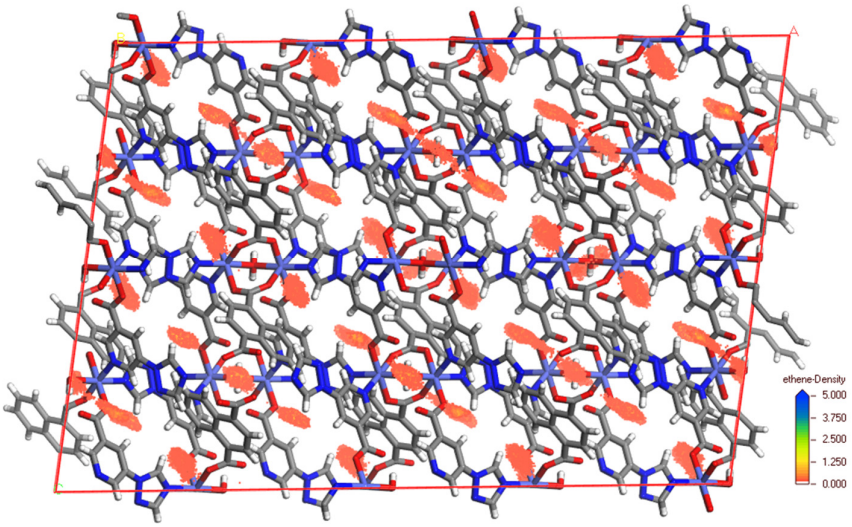

Figure S20. Density distribution of C_2H_4 in **NUM-18a** at 298 K and 1 bar.

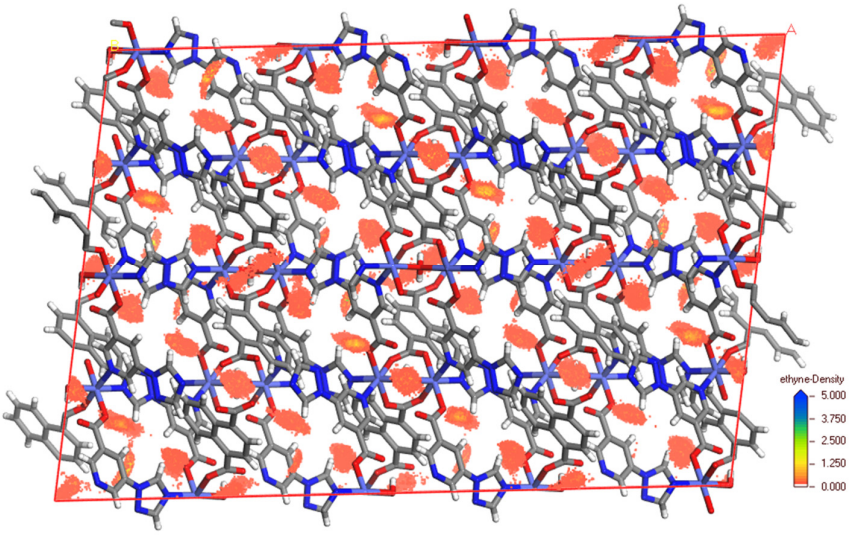

Figure S21. Density distribution of C_2H_2 in **NUM-18a** at 298 K and 1 bar.

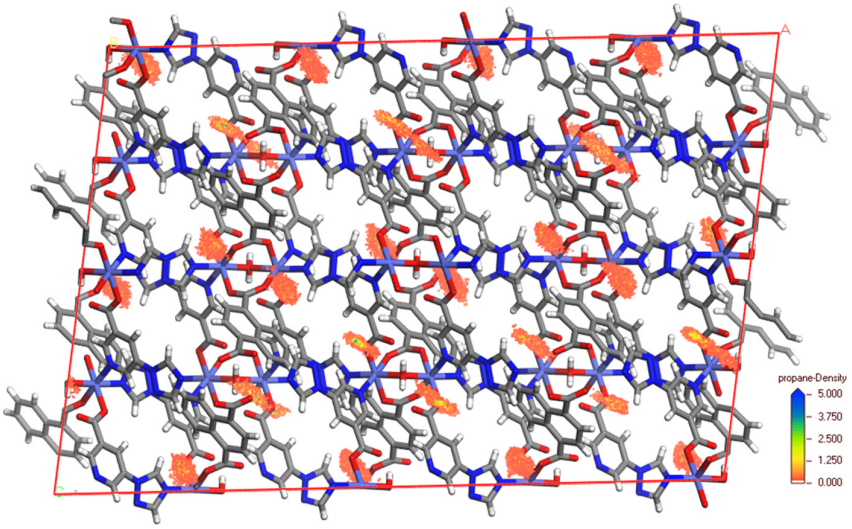

Figure S22. Density distribution of C_3H_8 in **NUM-18a** at 298 K and 1 bar.

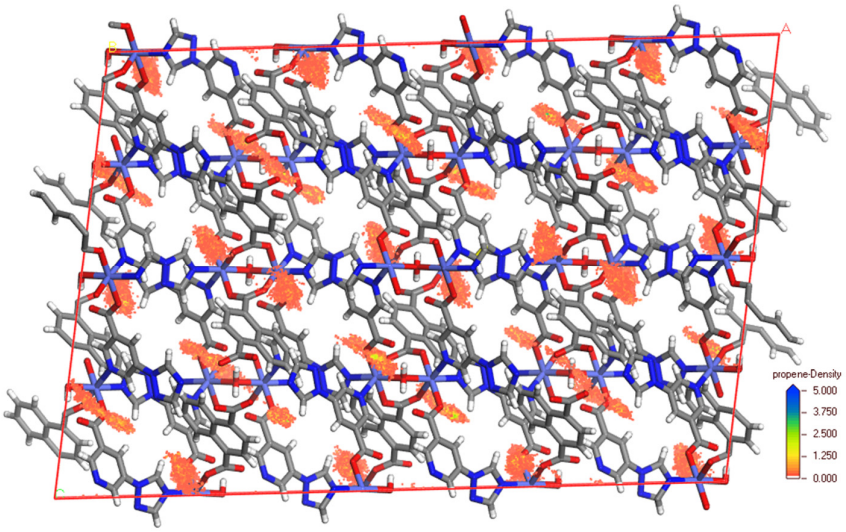

Figure S23. Density distribution of C_3H_6 in **NUM-18a** at 298 K and 1 bar.